

Peer review status:

This is a non-peer-reviewed preprint submitted to EarthArXiv.

Beyond the 100-kyr and 41-kyr dichotomy: ~ 76 -kyr and ~ 52 -kyr signals and forbidden periodicities

Takahito Mitsui

Faculty of Health Data Science, Juntendo University, Urayasu, Chiba,
279-0013, Japan.

Contact: takahito321@gmail.com.

Abstract

While the Mid-Pleistocene Transition (MPT) is often described as a shift from 41-kyr to ~ 100 -kyr glacial cycles, this binary perspective fails to capture the nuanced spectral evolution of Quaternary climate. Applying wavelet-based spectral analysis to benthic $\delta^{18}\text{O}$ records, we identify previously underappreciated signals— ~ 52 kyr before 1.2 Ma and ~ 76 kyr thereafter—marking the MPT’s onset. Insolation analysis reveals these timescales primarily correspond to integer multiples (n) of the local-mean climatic precession period (T_p), with minor modulation by obliquity. We further find that when T_p falls within this intermediate range (20.5–22 kyr), high eccentricity triggers deglaciation, precluding the emergence of 60–65 kyr and 100–110 kyr cycles. These findings refine the conventional “41-kyr to 100-kyr” paradigm, revealing an evolution from a quasi-41-kyr regime including ~ 52 -kyr cycles to a post-MPT regime of quantized ~ 76 , ~ 95 , and ~ 120 kyr cycles. This points to precession-based pacing as a persistent feature of Quaternary glacial dynamics.

Introduction

Glacial–interglacial cycles are the dominant mode of Quaternary climate variability, characterized by substantial fluctuations in temperature [1, 2], global ice volume [3], and atmospheric greenhouse gas concentrations [4, 5]. Benthic oxygen isotope ratios ($\delta^{18}\text{O}$) from marine sediments record past ice volume variations, although they are also influenced by deep-sea temperature and salinity [6] (Fig. 1d). Over the course of long-term Cenozoic cooling, the dominant periodicity of these cycles shifted from ~ 41

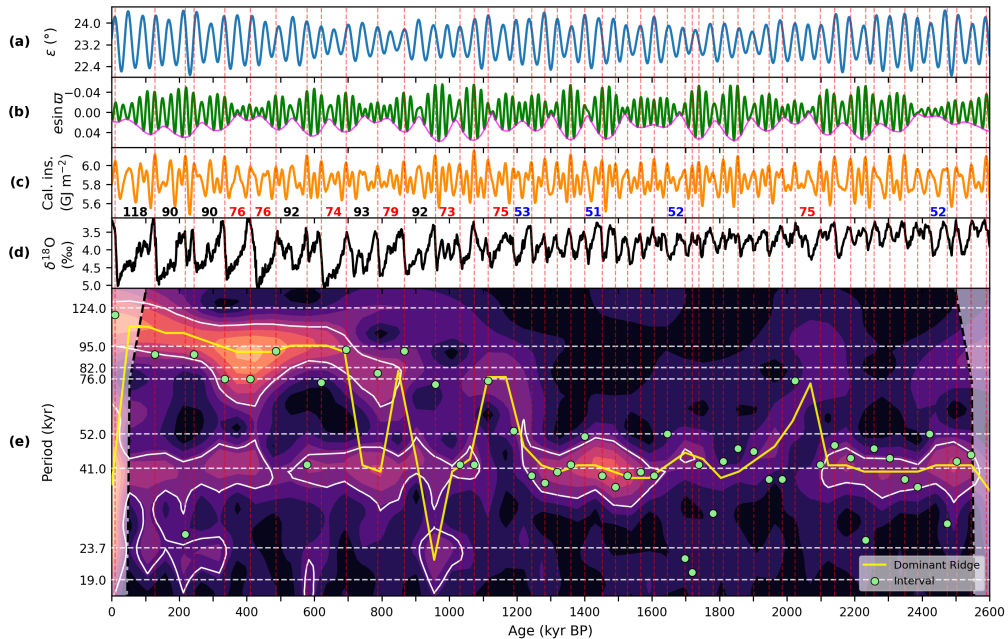


Fig. 1 Orbital forcing and wavelet analyses of the LR04 benthic $\delta^{18}\text{O}$ stack record over the last 2.6 Myr. (a) Obliquity (ε) [10]. (b) Climatic precession ($e \sin \omega$, green) and its eccentricity envelope (e , magenta) [10]. Note that negative values of climatic precession correspond to positive anomalies in Northern Hemisphere summer insolation. (c) Caloric summer half-year insolation at 65°N [11, 12]. (d) LR04 benthic $\delta^{18}\text{O}$ stack record [6]. Higher $\delta^{18}\text{O}$ values indicate larger ice volume and lower deep-ocean temperatures. (e) Wavelet power scalogram of the $\delta^{18}\text{O}$ record. The yellow line indicates the ridge of maximum wavelet power. Areas enclosed by white dashed lines indicate power significant at the 95% confidence level against an AR(1) benchmark. Horizontal dashed lines denote major astronomical periodicities, including the 76-kyr and 52-kyr scales discussed in this study. The vertical dashed lines indicate the timings of insolation peaks associated with interglacial onsets, as defined in Tzedakis et al. (2017) [13], across all panels. Spacings longer than 50 kyr between successive interglacial-inducing insolation peaks are labeled in panel (c). In panel (e), the green dots indicate the insolation-based interglacial spacing (T_{ins}) derived from these peaks.

30 kyr to ~ 100 kyr, accompanied by an increase in amplitude—a reorganization known
 31 as the Mid-Pleistocene Transition (MPT; 1.25–0.7 Ma) [7–9].

32 While the astronomical influence on glacial cycles via insolation forcing was pro-
 33 posed as early as the mid-19th century, it lacked robust observational support until
 34 the late 20th century [14]. Hays et al. (1976) [15] provided a breakthrough by per-
 35 forming spectral analysis of marine $\delta^{18}\text{O}$ records, identifying ~ 19 - and ~ 23 -kyr peaks
 36 corresponding to climatic precession (Fig. 1b) and a ~ 41 -kyr peak corresponding to
 37 obliquity (Fig. 1a) [10, 16]. This provided the compelling evidence that glacial cycles
 38 are paced by orbital forcing. However, the ultimate pacemaker of the ~ 100 -kyr cycles
 39 remains controversial; high-latitude summer insolation, considered crucial for the wax-
 40 ing and waning of continental ice sheets, lacks significant power within the ~ 100 -kyr
 41 band [14, 15]. Consequently, the ~ 100 -kyr cycles are often interpreted as nonlinear
 42 responses occurring once every four or five precession cycles [17–19] or every two or

43 three obliquity cycles [20–22]. It remains a matter of active debate whether precession
44 [19, 23–26], obliquity [20, 21], or a combination of both [13, 22, 27–29] predominantly
45 governs their timing, rhythm, and amplitude.

46 Many studies have investigated the triggers of deglaciations by relating their timing
47 to the phases of obliquity, precession, and various insolation metrics [19, 22, 26, 27, 30].
48 However, uniquely defining the timing of deglaciations is inherently challenging, as the
49 process sometimes spans multiple precession cycles and involves several discrete stages
50 of ice-sheet retreat (see below). Although spectral analysis avoids these timing ambi-
51 guities, it often lacks the resolution required to distinguish spectral peaks sufficiently
52 to resolve the precession-versus-obliquity debate at the ~ 100 -kyr scale.

53 Here, we revisit the spectral analysis of glacial-interglacial cycles using a weighted
54 wavelet spectral analysis method, originally developed by Foster (1996) as the
55 Weighted Wavelet Z-transform [31] and refined by Kirchner and Neal (2013) [32].
56 This approach estimates spectral power via a localized weighted least-squares pro-
57 jection (see Methods). Implemented via the Python package `Pyleoclim` [33], this
58 method resolves both the time-evolving nature of dominant periodicities (scalogram)
59 and the overall power spectral density (PSD) without requiring prior interpolation or
60 detrending. Beyond well-established spectral components, our analysis reveals a dis-
61 tinct ~ 76 -kyr peak (post-1.25 Ma) and a 52-kyr power band (pre-1 Ma) across multiple
62 benthic stacks—findings further corroborated by conventional spectral estimators.
63 Drawing on the theoretical framework of Tzedakis et al. (2017) [13], we interpret these
64 periodicities as robust evidence of nonlinear subharmonic (many-to-one) responses of
65 glacial cycles to climatic precession forcing.

66 Wavelet spectral analysis of benthic $\delta^{18}\text{O}$ records

67 Wavelet-based spectral analysis is performed on seven benthic $\delta^{18}\text{O}$ records (Fig. S1) to
68 investigate their periodicities under varying age-modeling constraints (see Methods).
69 First, we include the orbitally-tuned LR04 stack [6] (Fig. 1d) and its orbital-tuning-
70 free counterpart in Lisiecki (2010) [34]. Second, we analyze recent stack records in
71 Zhou et al. (2026) [35]: `BIGSTACKmixed` uses speleothem-based age constraints for
72 0–654 ka and tuning to an ice-sheet model for earlier intervals; `BIGSTACKmagrev` is
73 primarily constrained by paleomagnetic events to minimize orbital circularity; and
74 `BIGSTACKauto` is generated using an automated optimization algorithm [36] to min-
75 imally tune to the pervasive 41-kyr obliquity cycle, while avoiding assumptions about
76 astronomical phase relationships. Additionally, we utilize the orbitally-untuned ben-
77 thic stack record in Huybers (2007) [37] and the paleomagnetically-constrained record
78 U1476pMag from IODP Site U1476 [25]. To ensure the robustness of the detected peri-
79 odicities, we primarily focus on results from records with minimal or no orbital tuning
80 (Lisiecki 2010, `BIGSTACKmagrev`, Huybers 2007, and U1476pMag), while using the
81 fully tuned records as supplementary evidence.

82 The result of time-frequency analysis for the orbitally tuned LR04 record is shown
83 in Fig. 1e, with the yellow line tracking the instantaneous period at which the wavelet
84 amplitude is maximized (see Figs. S2–S7 for the other records). The evolution of the
85 dominant period in the seven records compared in Fig. 2 exhibits a broadly similar

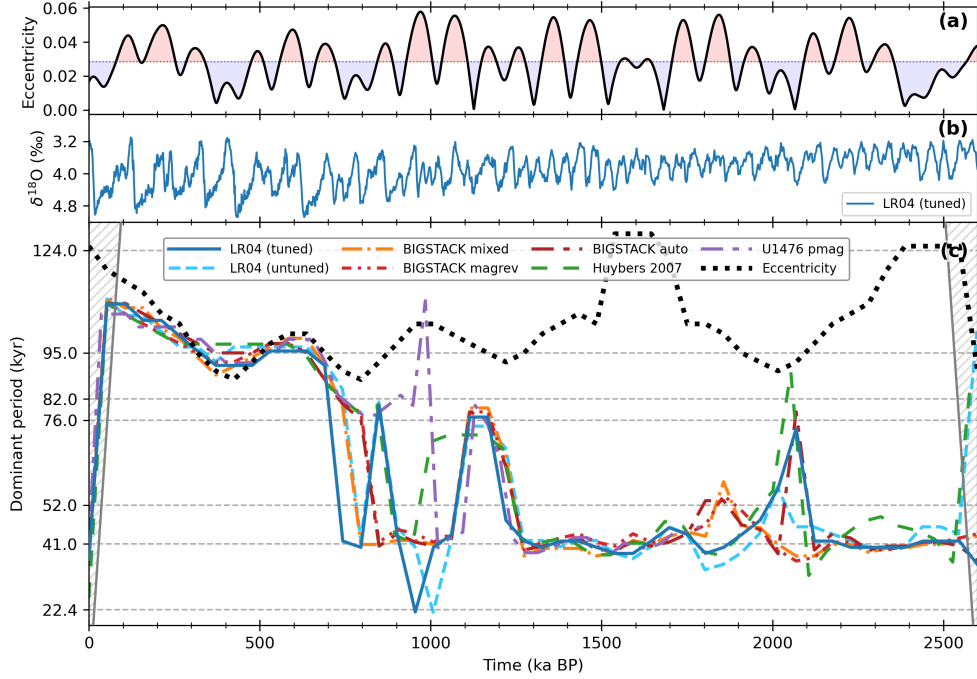


Fig. 2 Evolution of the dominant timescale of glacial cycles and that of eccentricity. (a) Eccentricity. The horizontal is the average. (b) LR04 benthic $\delta^{18}\text{O}$ stack. (c) Dominant timescale corresponding to the maximum wavelet amplitude at each time. Horizontal dashed lines denote major astronomical periodicities, including the 76-kyr and 52-kyr scales discussed in this study.

86 pattern across all analyzed records, although the MPT epoch (0.7–1.25 Ma) is notably
 87 complex, with marked discrepancies between records.
 88 Prior to the MPT, the dominant period remains centered near 41 kyr, although
 89 most records show transient increases in the primary period between 1.8 and 2.1 Ma
 90 (Fig. 2), with some variability in timing among the stacks. At the onset of the MPT,
 91 the dominant period increases up to ~ 76 kyr by ~ 1.2 Ma, a feature robust across
 92 records. However, this increase is interrupted around 1.1 Ma, and the subsequent
 93 evolution of the dominant period during 1.1–0.7 Ma varies significantly among the
 94 records. Notably, the dominant period retreats to ~ 22 kyr in the tuned and untuned
 95 LR04 records and to ~ 41 kyr in the other records at least once during 1.1–0.9 Ma.
 96 This transient reduction in period coincides with the strongest eccentricity maximum
 97 of the Quaternary. While the emergence of strong ~ 100 -kyr power after ~ 700 ka is well
 98 documented [38–40], our analysis uncovers a more nuanced progression. Specifically,
 99 the dominant period remains centered near ~ 95 kyr over 700–300 ka, after which it
 100 lengthens toward ~ 120 kyr (Fig. 2). The temporal evolution of the dominant period of
 101 ice age cycles closely follows that of eccentricity, excluding the ~ 400 -kyr component,
 102 suggesting the establishment of frequency locking between ice volume and ~ 100 -kyr-
 103 scale eccentricity cycles after the end of the MPT (~ 700 ka) (Fig. 2c).

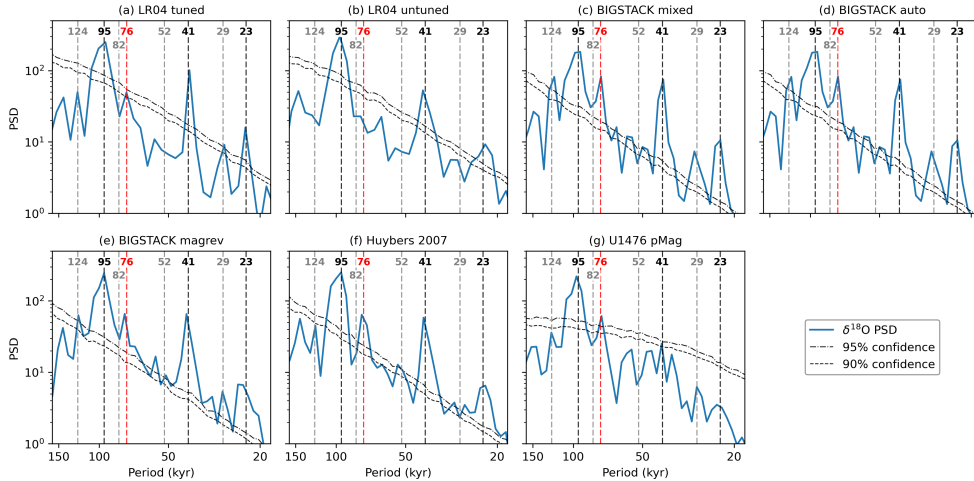


Fig. 3 Power spectral densities (PSD) of benthic $\delta^{18}\text{O}$ records over the last 1.25 Myr. (a) the tuned LR04 stack [6], (b) the untuned LR04 stack [34], (c) $\text{BIGSTACK}_{\text{mixed}}$ [35], (d) $\text{BIGSTACK}_{\text{auto}}$ [35], (e) $\text{BIGSTACK}_{\text{magrev}}$ [35], (f) the untuned record from Huybers (2007) [37], and (g) the U1476 record [25]. Solid blue lines denote the PSD of the $\delta^{18}\text{O}$ records, and dashed/dotted black lines indicate the 95% and 90% confidence levels against an AR(1) benchmark. Vertical dashed lines highlight key periodicities: eccentricity (124 and 95 kyr), obliquity (41 kyr), and climatic precession (23 kyr). Also indicated are the subharmonic of 41 kyr (82 kyr), the combination tone (29 kyr; $1/29 \approx 1/41 + 1/95$) [41], and specific timescales of interest in this study (76 and 52 kyr).

104 To assess the statistical significance of the observed periodicities, we calculate
 105 power spectral densities (PSDs) for the intervals before and after the MPT. For the
 106 mid-to-late Pleistocene (the past 1.25 Myr), 95-kyr, 41-kyr, and 23-kyr periodicities
 107 generally exhibit significant power at the 95% confidence level, although the latter two
 108 do not reach this level in the U1476 record (Fig. 3). Notably, we identify a spectral peak
 109 near ~ 76 kyr, which is significant in all records—including the orbitally tuned LR04
 110 (at the 90% level) and U1476—except for the untuned LR04. However, conventional
 111 periodograms (Fig. S9) reveal significant ~ 76 -kyr peaks across all records, including
 112 the untuned LR04. While this peak is less defined in Lomb–Scargle periodograms
 113 over the last 1.25 Myr, it becomes significant when the analysis is extended to the
 114 full Quaternary (2.6 Myr) except the untuned LR04 (Fig. S10). During the early-to-
 115 mid Pleistocene (1.0–2.6 Ma), the 41-kyr spectral peak is prominent across all records
 116 (Fig. 4). The tuned LR04 record further exhibits a significant peak at ~ 52 kyr, while
 117 the PSDs of $\text{BIGSTACK}_{\text{magrev}}$ and Huybers (2007) show a significant shoulder extend-
 118 ing from the 41-kyr peak toward this periodicity. A similar, though non-significant
 119 ($< 95\%$), feature is present in the untuned LR04. In contrast, no comparable 52-kyr
 120 power is observed in $\text{BIGSTACK}_{\text{mixed}}$, $\text{BIGSTACK}_{\text{auto}}$, and U1476pMag. Given that
 121 $\text{BIGSTACK}_{\text{auto}}$ and $\text{BIGSTACK}_{\text{magrev}}$ share the same $\delta^{18}\text{O}$ values but employ dif-
 122 ferent age-modeling strategies, it is possible that the ~ 52 -kyr power was suppressed
 123 or lost during the orbital tuning process to the 41-kyr obliquity cycles. Regarding
 124 U1476pMag, the absence of ~ 52 -kyr power likely stems from its relatively short record

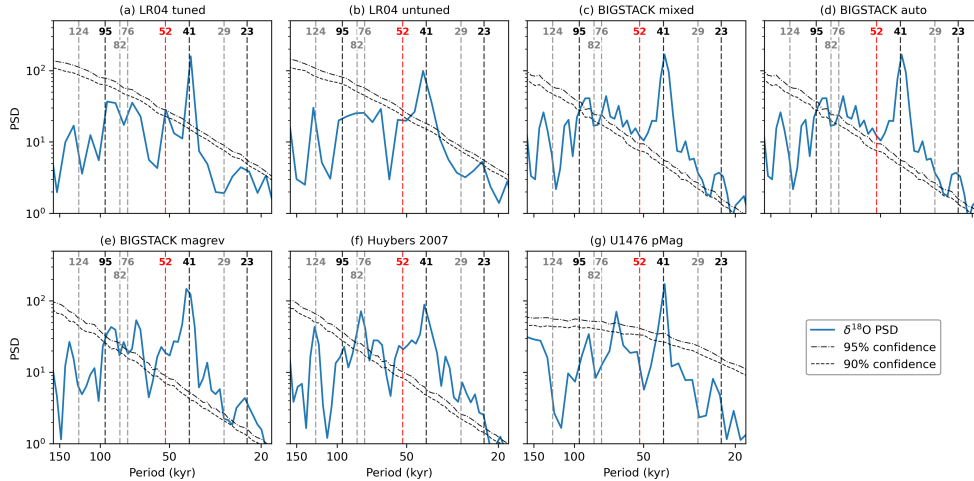


Fig. 4 Power spectral densities (PSD) of benthic $\delta^{18}\text{O}$ records over 1.0–2.6 Ma. (a) the tuned LR04 stack [6], (b) the untuned LR04 stack [34], (c) $\text{BIGSTACK}_{\text{mixed}}$ [35], (d) $\text{BIGSTACK}_{\text{auto}}$ [35], (e) $\text{BIGSTACK}_{\text{magrev}}$ [35], (f) the untuned record from Huybers (2007) [37], and (g) the U1476 record [25]. Solid blue lines denote the PSD of the $\delta^{18}\text{O}$ records, and dashed/dotted black lines indicate the 95% and 90% confidence levels against an AR(1) benchmark. Vertical dashed lines highlight key periodicities: eccentricity (124 and 95 kyr), obliquity (41 kyr), and climatic precession (23 kyr). Also indicated are the subharmonic of 41 kyr (82 kyr), the combination tone (29 kyr; $1/29 \approx 1/41 + 1/95$) [41], and specific timescales of interest in this study (76 and 52 kyr).

length (786.5 kyr), which limits the spectral resolution required to resolve such components. Consistently, alternative estimators—specifically conventional (Fig. S9) and Lomb-Scargle periodograms (Fig. S10)—detect the ~ 52 -kyr feature in most records, reinforcing its robust presence.

In summary, spectral power near ~ 76 kyr and ~ 52 kyr is reproducible across multiple datasets and estimation methods, though detectability varies with age modeling and tuning strategies. The ~ 76 -kyr peak is a consistent feature of late Pleistocene variability, while the ~ 52 -kyr feature—despite less consistent expression—appears to be a real component of early-to-mid Pleistocene variability rather than an analytical artifact. The lack of detection in the untuned LR04 likely reflects its conservative age constraints using only three tie points over the 2.6 Myr [34] (Methods), which may dampen these specific periodicities.

Interpretation of ~ 76 -kyr and ~ 52 -kyr components

We interpret the periodicities detected in the PSD in relation to insolation cycles, using the theoretical framework of interglacial spacing proposed by Tzedakis et al. (2017) [13] (T17). In this model, an interglacial occurs when the caloric summer half-year insolation peak at 65°N exceeds a threshold that declines with the time elapsed since the previous interglacial, reflecting the accumulated instability during the glacial period (Methods). Using this criterion, the model predicts which insolation peaks lead

144 to interglacials over the Quaternary (Fig. 1, vertical dashed lines). Though BIGSTACK
145 was recently published [35] as an update to LR04, we use LR04 in the following analysis
146 because the T17 model was calibrated using that stack.

147 We calculate proxy-based deglaciation spacings and insolation-based interglacial
148 spacings, demonstrating their overall consistency. Following T17, interglacials are iden-
149 tified in the LR04 record when $\delta^{18}\text{O}$ values fall below a predefined threshold (see
150 Methods). Near each threshold-crossing timing of $\delta^{18}\text{O}$, the timing of deglaciation
151 is specified as the peak in the derivative of the 10-kyr smoothed LR04 $\delta^{18}\text{O}$ record
152 (Figs. S11–S13). Some deglaciations span multiple precession cycles, leaving multiple
153 peaks in $\delta^{18}\text{O}$ derivative (e.g., deglaciations leading to MIS 13a near 500 ka as well
154 as MIS 17 near 700 ka in Fig. S11). We select the largest derivative peak within a
155 window of either ± 10 kyr or ± 15 kyr around each threshold-crossing point. The ± 10 -
156 kyr window tends to capture the later peak within a deglaciation sequence, whereas
157 the ± 15 -kyr window captures the earlier peak (Figs. S11–S13). The resulting spacings
158 between deglaciations, denoted T_{later} and T_{earlier} , are shown in Fig. 5. Furthermore, we
159 define insolation-based interglacial spacing (T_{ins}) as the intervals between successive
160 caloric summer insolation peaks that ultimately induced each interglacial [13] (Fig. 5;
161 Fig. 1e, green dots). The $\delta^{18}\text{O}$ -derivative-based intervals may tightly couple with the
162 periodicities detected in the PSD, but their values rely on an assumed age model. In
163 contrast, the insolation-based intervals are relatively free from chronological uncer-
164 tainties and can be directly linked to orbital cycles. See Supplementary Data S1 for
165 the values of T_{later} , T_{earlier} , and T_{ins} .

166 The high consistency among T_{later} , T_{earlier} , and T_{ins} shown in Fig. 5a ($r \gtrsim 0.95$,
167 RMSE $\lesssim 6.5$ kyr) supports T_{ins} as a reliable basis for analyzing glacial-cycle period-
168 icities. Although discrepancies of up to ~ 20 kyr exist for certain deglaciations—likely
169 reflecting the inherent uncertainty in deglaciation timing and the simplified nature
170 of the T17 model—the overall robustness of the correlation supports using T_{ins} for
171 interpreting the periodicities in the PSD.

172 The distribution of T_{ins} shows clear clustering around 90–93 kyr and 73–76 kyr
173 (Fig. 5e). A similar, albeit weaker, clustering is preserved in T_{earlier} (Fig. 5d). We,
174 therefore, attribute the ~ 95 -kyr spectral peak to the cluster of 90–93 kyr spacings, and
175 the ~ 76 -kyr spectral peak to the 73–76 kyr cluster. Before the MPT (~ 1.2 Ma), T_{ins}
176 is distributed around the 41-kyr obliquity period with a mean of 41.2 kyr, contributing
177 to the dominant 41-kyr peak. However, its standard deviation is substantial (± 10 kyr).
178 Indeed, four spacings fall within 51–53 kyr (Figs. 1e, 5e), contributing to the significant
179 ~ 52 -kyr peak in the PSD of the LR04 record over 1.0–2.6 Ma (Fig. 4a).

180 Once linked with T_{ins} , the observed spectral peaks can be traced back to their
181 physical origins by decomposing the insolation forcing into climatic precession and
182 obliquity components. A key factor in considering the variability of T_{ins} is that the
183 duration of climatic precession cycles varies widely between 14 and 31 kyr when eccen-
184 tricity is low, whereas it remains relatively stable around 22.1 kyr when eccentricity
185 is high (Fig. S14) [42]. Indeed, the length of the late-Pleistocene glacial cycles is
186 explained with the varying durations of climatic precession cycles [19]. Building on
187 this, we derive more refined relationships between T_{ins} and the evolving durations of
188 precession and obliquity cycles.

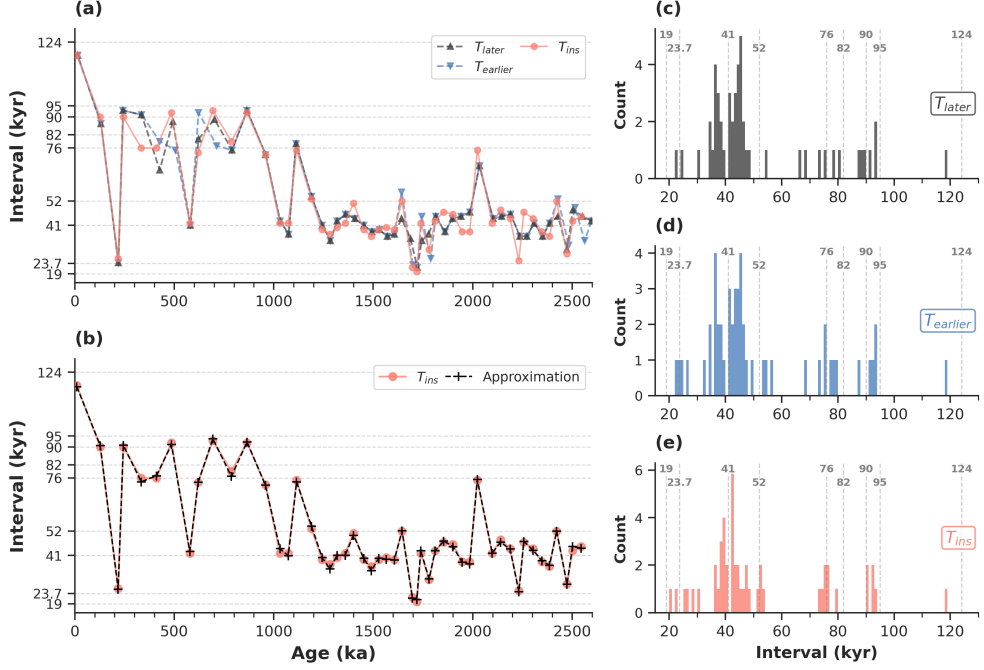


Fig. 5 Comparison of proxy-based deglaciation spacings and insolation-based interglacial spacings. (a) Time series of spacings over the past 2600 kyr. These intervals are defined by three different metrics: orbital insolation peaks (T_{ins} , salmon circles) and the timing of peak deglaciation rates (T_{later} , dark blue triangles; $T_{earlier}$, light blue inverted triangles). Horizontal dashed lines indicate key orbital periodicities and the sub-harmonic periodicities discussed in this study (52, 76, and 82 kyr). (b) Comparison between the insolation-based spacings (T_{ins}) and their theoretical approximation (black crosses). (c)–(e) Frequency distributions (histograms) of (c) T_{later} , (d) $T_{earlier}$, and (e) T_{ins} . The insolation-based distribution (e) exhibits distinct clustering around 73–76 kyr and 90–93 kyr; this pattern is partially reflected in the $T_{earlier}$ and T_{later} metrics. All proxy-based metrics align well with T_{ins} ($r \gtrsim 0.95$, $RMSE \lesssim 6.5$ kyr), justifying the use of T_{ins} as a robust theoretical framework for spectral analysis.

189 For each glacial cycle, we approximate the local variations in the caloric summer
 190 half-year insolation as $f(t) = A_p \cos(\omega_p t + \varphi_p) + A_o \cos(\omega_o t + \varphi_o)$, accounting for the
 191 respective positive contributions of climatic precession and obliquity to the insolation.
 192 Here, $A_{p,o}$ are the local-mean amplitudes, $\omega_{p,o}$ are the angular frequencies (correspond-
 193 ing to local-mean periods $T_{p,o}$), and $\varphi_{p,o}$ are the local phases of climatic precession
 194 and obliquity cycles. Unless otherwise noted, we can choose $A_{p,o} = 1$ for 65°N caloric
 195 summer insolation, as climatic precession and obliquity contribute nearly equally to
 196 the total variance [11]. The local-mean periods T_p (T_o) are calculated from the time
 197 intervals between successive precession minima (obliquity maxima) associated with
 198 deglaciations (Figs. S15–S18; Data S1). The local phases $\varphi_{p,o}$ are chosen from the dis-
 199 crete set $\{0, \pm\pi/2, \pi\}$ for simplicity, to best capture local insolation variations. Then,
 200 we obtain approximation formulae for T_{ins} as follows.

Here we present two representative cases (all derivations are provided in the Supplementary Information). When the peaks of climatic precession and obliquity nearly coincide and collectively induce an interglacial, we define this peak time as $t = 0$ by setting $\varphi_p = \varphi_o = 0$ (Fig. S19a). If the spacing T_{ins} between the peak at $t = 0$ and a subsequent interglacial-inducing peak is close to the n -th multiple of the local-mean precession period T_p , it can be expressed as $T_{\text{ins}} = nT_p + \delta$. Here, δ represents a small temporal shift relative to the nominal insolation peak, originating from the modulation by obliquity. By linearizing the peak condition as $f'(nT_p + \delta) \approx f'(nT_p) + f''(nT_p)\delta = 0$, we obtain approximation formulæ for T_{ins} ($n = 2, 3, 4, 5$), called type-a:

$$T_{\text{ins}} \approx nT_p - \frac{A_o \omega_o \sin(n\omega_o T_p)}{A_p \omega_p^2 + A_o \omega_o^2 \cos(n\omega_o T_p)}.$$

201 An example of type-a is the ~ 76 -kyr spacing between interglacials MIS 11c and MIS 9e
 202 (Fig. S15), where the corresponding insolation peaks are separated by approximately
 203 four precession cycles ($n = 4$), and the local-mean precession period is $T_p = 18.25$ kyr.
 204 Furthermore, the local-mean obliquity period is $T_o = 41.5$ kyr. The type-a formula
 205 then predicts $T_{\text{ins}} = 74.3$ kyr. This value is closer to the actual value of 76 kyr than the
 206 simple multiple of precession, $nT_p = 73$ kyr, obtained without the shift $\delta = 1.43$ kyr.

The second case occurs when a glacial cycle spans roughly three precession cycles ($n = 3$); here, the insolation is locally approximated as $f(t) = -A_p \cos(\omega_p t) - A_o \cos(\omega_o t)$ over the interval $-\frac{3}{2}T_p \lesssim t \lesssim \frac{3}{2}T_p$ corresponding to $\varphi_p = \varphi_o = \pi$ (Fig. S19b). For this case, we assume that deglaciations occur at $t = \pm(\frac{3}{2}T_p + \delta)$, with δ being a small obliquity-induced shift. Following a derivation similar to that of the type-a formulæ, T_{ins} is given by the following formula (type-3b):

$$T_{\text{ins}} \approx 3T_p + \frac{2A_o \omega_o \sin(\frac{3}{2}\omega_o T_p)}{A_p \omega_p^2 - A_o \omega_o^2 \cos(\frac{3}{2}\omega_o T_p)}.$$

207 An example of type-3b is the spacing between interglacials MIS 37 and MIS 35
 208 (Fig. S16). The corresponding insolation peaks are separated by approximately three
 209 precession cycles, and the local-mean precession period is $T_p = 19$ kyr. Furthermore,
 210 the local-mean obliquity period is $T_o = 39$ kyr. Then, the type-3b formula predicts
 211 $T_{\text{ins}} = 54.2$ kyr. This value is closer to the actual value of 53 kyr than the simple
 212 multiple of precession, $nT_p = 57$ kyr, obtained without the shift $\delta = -2.8$ kyr.

213 In this manner, by varying the number of precession cycles (n) and the local
 214 phases $\varphi_{p,o}$, we derive twelve distinct formulæ (e.g., types 2a–5a, 1b–4b, 1c–2c, 2d,
 215 and pp). The detailed derivation of each formula is presented in the Supplementary
 216 Information, along with a one-to-one correspondence to each individual glacial cycle
 217 (Table S1). These analytical expressions account for nearly 50 interglacial spacings
 218 identified throughout the Quaternary. While we generally use a fixed amplitude ratio
 219 of $A_p/A_o = 1$ for simplicity, we explicitly consider the relative amplitudes in two
 220 specific cases of extremely low eccentricity (MIS 99–97 and MIS 97–95). Similarly, the
 221 intervals MIS 95–93 and MIS 93–91 represent epochs in which eccentricity remains
 222 near zero. The aforementioned formulæ are inapplicable to these events as deglaciation
 223 aligns with the obliquity maximum at 2386 ka, where eccentricity is virtually zero. For

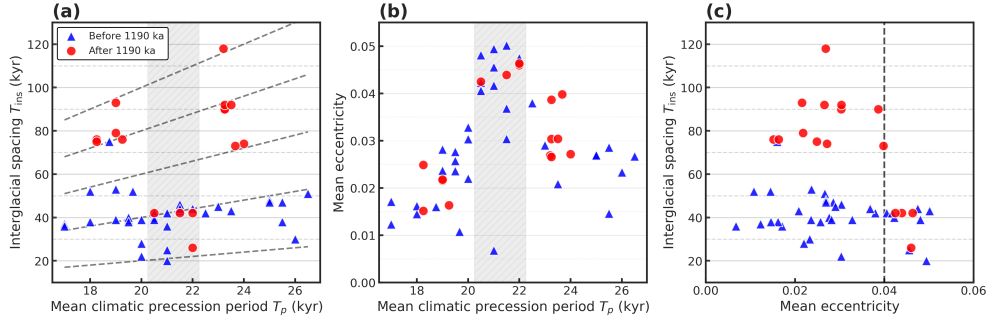


Fig. 6 Statistical relationships between orbital parameters and interglacial spacings. (a) Mean climatic precession period (T_p) versus the insolation-based interglacial spacing (T_{ins}). Dashed lines represent integer multiples of T_p ($T = nT_p$ for $n = 1, \dots, 5$), showing the clustering of interglacial spacing. (b) T_p versus the mean eccentricity (\bar{e}) over each interval. In (a) and (b), the vertical hatched area (20.25–22.25 kyr) indicates the range of climatic precession periods where high mean eccentricity generally prevents the skipping of precession peaks. (c) Mean eccentricity versus T_{ins} . The vertical dashed line at $\bar{e} = 0.04$ indicates the threshold below which peak-skipping (longer T_{ins}) becomes frequent. In all panels, blue triangles and red circles represent intervals before and after 1190 ka, respectively.

224 these two cases, we employ exceptional but simplified estimates for T_{ins} , the details of
 225 which are described in the Supplementary Information. The validity of this analytical
 226 framework is confirmed by its high predictive power; across the entire Quaternary,
 227 these formulae approximate T_{ins} with a mean absolute error of only 0.8 kyr (Fig. 5b).

228 Precession phase-locking and forbidden periodicities

229 It is found that the shift δ in the approximation $T_{\text{ins}} = nT_p + \delta$ has standard deviation
 230 of only 2.7 kyr. Consequently, the insolation-based interglacial spacings T_{ins} cluster
 231 along the lines $T_{\text{ins}} = nT_p$ ($n = 1, 2, 3, 4, 5$) as functions of the local-mean precession
 232 period T_p (Fig. 6a). The number of precession cycles within each interglacial spacing,
 233 n , can be explained by the T17 theory [13], where a longer spacing $T_{\text{ins}} (\approx nT_p)$
 234 facilitates crossing the deglaciation threshold due to the accumulated instability of the
 235 ice sheet–climate system due to the accumulated instability of the ice sheet–climate
 236 system (see Methods). After the onset of the MPT around 1.2 Ma, n statistically
 237 increases as a result of an elevated deglaciation threshold, and the points (T_p, T_{ins})
 238 tend to cluster along higher branches with $n \geq 3$.

239 Figure 6a reveals that similar interglacial spacings (T_{ins}) can arise from different
 240 precession-cycle lengths (T_p). For instance, the 90–93 kyr spacings comprise either four
 241 precession cycles with a mean period of $T_p \approx 23$ kyr or five cycles with a mean period
 242 of $T_p \approx 19$ kyr. Similarly, the 73–76-kyr spacings comprise either three precession
 243 cycles with a mean period of $T_p \approx 24$ kyr or four precession cycles with a mean
 244 period of $T_p \approx 19$ kyr. A similar bifurcation is observed for the 51–53-kyr spacings,
 245 which split into two distinct solutions: three multiples of precession cycles with a mean
 246 period of $T_p \approx 19$ kyr and two multiples of precession cycles with a mean period of
 247 $T_p \approx 26.5$ kyr. The points in ~ 41 -kyr cluster distribute along $T_{\text{ins}} = 2T_p$ (Fig. 6a, the

248 second dashed line from the bottom), showing the persistent influence of precession
249 cycles across the MPT, as suggested in previous studies [25, 43–45].

250 Interestingly, when the mean climatic precession period T_p falls between 20.5 and
251 22 kyr, glacial cycles longer than 50 kyr are notably absent (shaded region, Fig. 6a).
252 This gap occurs because this intermediate T_p range coincides with periods of high
253 mean eccentricity ($\bar{e} > 0.04$) both after and, in many cases, before the MPT’s onset
254 (~ 1.2 Ma) (Fig. 6b). Under these conditions of high eccentricity, the amplified climatic
255 precession forcing ensures that summer insolation remains sufficiently high to trigger
256 deglaciation within one or two precession cycles (Fig. 6c), thereby precluding longer
257 cycles. This orbital constraint provides a physical basis for the distinct gaps observed
258 in the spacing histograms (Figs. 5c–5e), explaining why certain durations— ~ 60 – 66
259 kyr (3×20 to 3×22) and ~ 100 – 110 kyr (5×20 to 5×22)—are effectively precluded.

260 Discussion

261 We show that glacial cycles evolved from a quasi-41-kyr regime characterized by large
262 variability—including ~ 52 -kyr cycles—to quantized ~ 76 , ~ 95 , and ~ 120 -kyr cycles.
263 This points to precession-based pacing as a persistent feature of glacial dynamics
264 throughout the Quaternary. Following the onset of the MPT (~ 1.2 Ma), ~ 76 -kyr cycles
265 emerged, coinciding with the disappearance of the ~ 52 -kyr periodicity. After the first
266 ~ 92 -kyr cycle appeared at ~ 0.9 Ma, the dominant period stabilized around ~ 95 kyr
267 from ~ 700 to ~ 300 ka, before eventually lengthening toward ~ 120 kyr. This temporal
268 evolution of the dominant period closely tracks the ~ 100 -kyr eccentricity component
269 (excluding the 400-kyr cycle), suggesting that frequency-locking between ice volume
270 and eccentricity was established after the end of the MPT (~ 700 ka; Fig. 2c). Such
271 resonance between the internal climate response and orbital forcing may explain the
272 abrupt increase in 100-kyr cycle amplitude observed at approximately 650 ka [38].

273 While the prominence of the ~ 76 -kyr periodicity has been noted in several studies
274 [19, 46, 47], its physical origin has remained elusive. For instance, Bolton et al. (1995)
275 [46] identified ~ 75 -kyr power around 750 ka but attributed it to internal variability,
276 citing the lack of a corresponding periodicity in the astronomical forcing. Rial (1999)
277 [47] proposed that the ~ 75 -kyr peak is a sideband frequency ($1/77 \approx 1/95 + 1/413$)
278 generated by frequency modulation of the 95-kyr cycle by the 413-kyr eccentricity
279 component; however, the physical basis for such modulation remains elusive. In
280 contrast, our results demonstrate that the ~ 76 -kyr spectral power arises from sub-
281 harmonic phase-locking to either three precession cycles (mean period $T_p \approx 24$ kyr)
282 or four precession cycles ($T_p \approx 19$ kyr), with only a minor contribution from obliq-
283 uity modulation. Consistently, Blackburn et al. (2024) [19] attributed the spacings
284 from MIS 13a to 11c and 11c to 9e to the 76-kyr mode of four precession cycles. This
285 precession-based 76-kyr mode is distinct from the previously proposed ~ 70 -kyr vari-
286 ability, which was interpreted as a beat frequency between obliquity and eccentricity
287 ($1/70 \approx 1/41 - 1/100$) [41]. Within our present same framework, the ~ 95 -kyr spectral
288 power can also be explained as a result of subharmonic phase-locking to either four
289 ($T_p \approx 23$ kyr) or five ($T_p \approx 19$ kyr) precession cycles [17–19, 23, 26, 48].

290 While the dominant power prior to the MPT is often characterized as ~ 41 kyr [49],
 291 this represents only a statistical average. In reality, interglacial spacings exhibit large
 292 variations of ~ 10 kyr around this mean because they correspond to either two or three
 293 multiples of climatic precession cycles, whose periods themselves vary significantly.
 294 Such variability in glacial duration is indeed reproduced in a mathematical model or
 295 a climate-ice sheet model [44, 50]. Our analysis identifies the ~ 52 -kyr-scale spectral
 296 shoulder extending from the 41-kyr peak as a diagnostic signature of this precessional
 297 influence prior to the onset of the MPT (~ 1.2 Ma). Previous research [41] attributed
 298 the spectral peaks near 50 kyr and 55 kyr to an eccentricity overtone ($1/50 = 2/100$
 299 kyr^{-1}) and an obliquity sideband, respectively. In contrast, we focus on the 51–53 kyr
 300 band and attribute its origin to a nonlinear subharmonic response. This is character-
 301 ized by two distinct solutions: the system responding once for every three precessional
 302 cycles of a mean period of $T_p \approx 19$ kyr or once for every two cycles of a mean period
 303 of $T_p \approx 26.5$ kyr.

304 The presence of bundles of precession cycles— ~ 52 -kyr cycles before ~ 1.2 Ma,
 305 ~ 76 -kyr cycles after ~ 1.2 Ma, and ~ 95 -kyr cycles after ~ 0.9 Ma—throughout the
 306 Pleistocene suggests that the MPT was not a disappearance of the obliquity-driven 41-
 307 kyr world, but rather a progressive shift in the skipping behavior of precession-paced
 308 deglaciations. This persistent influence of precession cycles both before and after the
 309 MPT is consistent with recent findings [25, 43–45, 51].

310 Consequently, the MPT can be understood as a period-adding process in
 311 precession-phase locking, driven by a gradual increase in the deglaciation threshold
 312 in the coupled ice-sheet–ocean–carbon system. The threshold likely increased grad-
 313 ually through long-term global cooling, declining atmospheric CO_2 toward critical
 314 minima [52–54], and structural changes in the cryosphere system including progressive
 315 removal of subglacial regolith beneath Northern Hemisphere ice sheets [54–56], expan-
 316 sion of marine-based Antarctic ice sheets [57], long-term AMOC slowdown [58], and
 317 enhanced stratification of the Southern Ocean [59]. These processes may have con-
 318 tributed to increasing the intrinsic timescale of the climate–ice-sheet system [28, 60],
 319 although their relative roles and interactions remain poorly constrained. Identifying
 320 the underlying physical mechanisms of the MPT is beyond the scope of this study.

321 We found that when the local-mean precession period T_p falls within this inter-
 322 mediate range (20.5–22 kyr), high eccentricity triggers deglaciation, precluding the
 323 emergence of ~ 100 –110-kyr and ~ 60 –65-kyr cycles. This is consistent with previous
 324 findings of an anticorrelation between ~ 100 -kyr eccentricity power and ~ 100 -kyr ice-
 325 age power [44, 61]. Our analysis shows that mean eccentricity does not exceed 0.04
 326 during the observed ~ 100 -kyr cycles (Fig. 6c). This implies that the development of
 327 ~ 100 -kyr cycles was precluded during the high-eccentricity interval between ~ 950 and
 328 1100 ka. Consequently, the onset of the MPT—specifically the lengthening of glacial
 329 cycles—appears to have been constrained by the long-term evolution of eccentricity
 330 [9, 44].

331 Our findings refine the conventional paradigm of a simple transition from a 41-
 332 kyr world to a 100-kyr world across the MPT. Instead, we propose a more nuanced
 333 evolution: from a quasi-41-kyr regime characterized by high orbital variability to a
 334 suite of quantized cycles (~ 76 , ~ 95 , and ~ 120 kyr) linked to precession phases. In

335 this framework, obliquity determines which climatic precession peaks are skipped, as
336 suggested in several studies [13, 19, 27, 28].

337 Methods

338 Benthic $\delta^{18}\text{O}$ records

339 We analyze seven benthic $\delta^{18}\text{O}$ records (Fig. S1) categorized by their degree of orbital
340 tuning. The first is the standard, orbitally-tuned LR04 stack [6] (Fig. 1d). The sec-
341 ond is the tuning-free version of the LR04 stack from Lisiecki (2010) [34], which
342 assumes a constant sedimentation rate between three primary tie points: the core top
343 (0 ka) and the geomagnetic reversals at 0.78 and 2.58 Ma. Third through fifth, we uti-
344 lize three versions of the BIGSTACK from Zhou et al. (2026) [35]: $\text{BIGSTACK}_{\text{mixed}}$
345 integrates 221 global records using speleothem-based age constraints for 0–654 ka
346 and ice-sheet model tuning for earlier intervals. $\text{BIGSTACK}_{\text{magrev}}$ (comprising 33
347 records) is constrained by 15 paleomagnetic events over the last 2.606 Ma to minimize
348 orbital circularity. $\text{BIGSTACK}_{\text{auto}}$ is derived from $\text{BIGSTACK}_{\text{magrev}}$ by applying the
349 eTimeOpt algorithm [36, 62] to minimally tune the pervasive 41-kyr obliquity signal
350 without assuming astronomical phase relationships. The sixth record is the depth-
351 derived stack of Huybers (2007) [37]. While the original study focuses on the last 2 Ma,
352 the dataset provides a tuning-free chronology anchored to the 2.58 Ma geomagnetic
353 boundary (<https://doi.org/10.25921/d1zr-t492>, last accessed 8 April 2026). Lastly, we
354 include the single-site benthic $\delta^{18}\text{O}$ record from IODP Site U1476, anchored to an
355 independent paleomagnetic age model (U1476pMag) [25]. Because this record spans
356 only the last 1786.542 kyr, its coverage of the pre-MPT interval (1.0–1.79 Ma) is rel-
357 atively short. Consequently, the presence or absence of periodicities in this specific
358 epoch should be interpreted with caution due to the limited duration of the time series.

359 In our spectral analysis, periodicities are primarily accepted based on the tuning-
360 free records (Lisiecki 2010, Huybers 2007, and U1476pMag) and the minimally-tuned
361 $\text{BIGSTACK}_{\text{magrev}}$. The orbitally-tuned records (standard LR04, $\text{BIGSTACK}_{\text{mixed}}$,
362 and $\text{BIGSTACK}_{\text{auto}}$) are used as supplementary evidence to support the robustness
363 of the detected signals.

364 Wavelet-based spectral analysis

365 Paleoclimate time series are commonly unevenly sampled, which complicates the
366 application of conventional spectral estimators, such as the periodogram [63] and
367 the multitaper method spectrum [64]. Standard approaches often rely on interpola-
368 tion to a regular time grid prior to analysis; however, such interpolation acts as a
369 low-pass filter, leading to a reddening of the power spectrum and, consequently, spu-
370 rious results in hypothesis testing [65]. While the Lomb–Scargle periodogram [66, 67]
371 avoids interpolation, it is known to overestimate power at high frequencies [65]. More-
372 over, Fourier-based methods, which assume stationarity, necessitate data detrending
373 [68]. However, even with recent methodological advances, identifying and removing a
374 trend without inadvertently compromising the underlying climate signal remains an
375 inherently difficult task [69].

376 To overcome these difficulties, we employ a weighted wavelet spectral analysis
377 method. This approach, originally developed by Foster (1996) [31] as the Weighted
378 Wavelet Z-transform (WWZ) and subsequently refined by Kirchner and Neal (2013)
379 [32], estimates spectral power via weighted least-squares projection. This approach,
380 implemented in the Python package `Pyleoclim` [33], enables the resolution of both
381 the time-evolving nature of dominant periodicities (scalograms) and the overall fre-
382 quency content (power spectral density; PSD) without requiring prior interpolation
383 or detrending.

384 The method estimates time-dependent harmonic amplitudes (a_1, a_2) through local-
385 ized fits of sinusoidal functions and a constant to the data using weighted least squares
386 [32]. Specifically, for each center time t^* and angular frequency ω , the coefficients a_1
387 and a_2 are obtained by fitting: $x_i = a_0 + a_1 \cos[\omega(t_i - t^*)] + a_2 \sin[\omega(t_i - t^*)]$, where each
388 observation x_i at time t_i is weighted by a Gaussian weight $w_i = \exp[-c\omega^2(t_i - t^*)^2]$,
389 with a decay constant c controlling the time-frequency resolution trade-off. However,
390 when the data are unevenly sampled in time, the basis functions can be non-orthogonal
391 (e.g., $\sum_i \cos[\omega(t_i - t^*)] \sin[\omega(t_i - t^*)] \neq 0$), which can lead to significant errors in esti-
392 mating the coefficients. To address this, Kirchner and Neal (2013) employ shifted basis
393 functions such that: $x_i = b_0 + b_1 \cos[\omega(t_i - \tau)] + b_2 \sin[\omega(t_i - \tau)]$, where the time shift
394 τ is chosen to ensure that the basis functions 1, $\cos[\omega(t_i - \tau)]$, and $\sin[\omega(t_i - \tau)]$ are
395 mutually orthogonal. The coefficients b_0, b_1 , and b_2 obtained via weighted regression
396 are then converted back to the original coefficients a_0, a_1 , and a_2 by accounting for
397 the phase shift $\omega(t^* - \tau)$.

398 The local spectral power, or scalogram, is calculated at each t^* as: $S_{\text{loc}}(t^*, \omega) =$
399 $\frac{1}{2}(a_1^2 + a_2^2)(t_{\text{max}} - t_{\text{min}}) \frac{n_{\text{eff}}}{n}$, where $t_{\text{max}} - t_{\text{min}}$ is the total time interval covered
400 by the n samples, and $n_{\text{eff}} = (\sum_i w_i)^2 / \sum_i w_i^2$ represents the effective number of
401 points. Finally, a robust global estimate of the Power Spectral Density (PSD) is
402 obtained by averaging the local spectral power over the entire time interval, as
403 $S(\omega) = \sum_{t^*} v_{\text{eff}}(t^*) S_{\text{loc}}(t^*, \omega) / \sum_{t^*} v_{\text{eff}}(t^*)$, where $v_{\text{eff}}(t^*) = \max\{0, n_{\text{eff}} - 3\}$ is the
404 effective degrees of freedom [32].

405 The decay constant c determines the frequency resolution in the spectral analysis
406 and balances the frequency and time resolution in the time-frequency analysis. For
407 the time-frequency analysis (scalogram), we adopt $c = 1/(8\pi^2)$, the standard value for
408 this analysis in `Pyleoclim` [33], which provides a balanced resolution for identifying
409 transient shifts in ice age periodicity. For the global spectral analysis (PSD), we set
410 $c = 0.0005$. This corresponds to a broader effective time window (slightly smaller than
411 the default value 0.001 in `Pyleoclim`) to prioritize high frequency resolution.

412 To check the sensitivity of our results, we conduct spectral analyses using multiple
413 estimators: the conventional periodogram [63] and the Lomb-Scargle periodogram [66,
414 67]. For the former, the time series is interpolated at 1-kyr intervals. In both cases,
415 the series are linearly detrended over the analysis period. All analyses are performed
416 using the `pyleoclim` (version 1.2.0) [33].

417 Interglacial spacings in Tzedakis et al. (2017)

418 Tzedakis et al. (2017) proposed a simple rule to determine which insolation peaks
419 trigger interglacials [13]. In their model, 51 interglacials are identified over the Qua-
420 ternary based on the LR04 benthic $\delta^{18}\text{O}$ stack [6], supported by additional composite
421 records from Eastern Equatorial Pacific sites. An interglacial onset is defined when the
422 detrended $\delta^{18}\text{O}$ value falls below a lower threshold of 3.68 ‰ after having exceeded a
423 higher threshold of 3.92 ‰. To apply this criterion consistently, $\delta^{18}\text{O}$ values prior to
424 1.5 Ma are detrended as $\delta^{18}\text{O}_{\text{detrended}} = \delta^{18}\text{O} + 3.296 \times 10^{-4}(t - 1500)$, where t is
425 the time in kyr, while values after 1.5 Ma remain unchanged. This trend is attributed
426 to the long-term cooling of deep-water temperatures or an increase in Antarctic ice
427 volume.

428 The T17 model predicts interglacial onsets based on caloric summer half-year
429 insolation. This measure represents the total insolation integrated over the caloric
430 summer half-year, which is defined such that every day within this period receives
431 more insolation than any day in the winter half [11, 12]. At 65°N, the variance of this
432 insolation measure receives approximately equal contributions from climatic preces-
433 sion and obliquity. In the T17 framework, an interglacial is triggered when a peak in
434 the 65°N caloric summer insolation exceeds a threshold that decreases as a function
435 of the time elapsed since the previous interglacial (Δt), reflecting the accumulation
436 of glacial instability. This condition can be expressed as the effective energy, defined
437 as $E(I_{\text{peak}}, \Delta t) = I_{\text{peak}} + b\Delta t$, exceeding a constant deglaciation threshold $I_{\text{threshold}}$.
438 Here, $b = 0.0021 \pm 0.0001 \text{ GJ m}^{-2} \text{ kyr}^{-1}$, and $I_{\text{threshold}}$ is defined to ramp up from
439 6.02 GJ m^{-2} to 6.14 GJ m^{-2} over the interval from 1.55 Ma to 0.61 Ma. Using this
440 criterion, the model can predict most of 51 interglacial onsets, with only two false
441 negatives (MIS 59 and 63). For these false negatives, the insolation peaks immedi-
442 ately preceding their respective isotopic minima are assumed to be the trigger. In the
443 present work, the interglacial spacings (T_{ins}) are defined as the durations between suc-
444 cessive caloric summer insolation peaks that finally induced each interglacial. Using
445 the T17, the interglacial spacing T_{ins} is determined as the minimal peak-to-peak spac-
446 ing that satisfies the condition $E(I_{\text{peak}}, T_{\text{ins}}) = I_{\text{peak}} + bT_{\text{ins}} > T_{\text{threshold}}$. Therefore,
447 $n = \text{argmin}_{\tilde{n} \geq 1} \{I_{\text{peak}} + b(\tilde{n}T_p + \delta) > T_{\text{threshold}}\}$.

448 **Supplementary information.** This article accompanies Supplementary Informa-
449 tion (Supplementary notes, Figures S1–S19, and Table S1).

450 **Acknowledgements.** The author thanks Prof. Polychronis Tzedakis and Prof. Eric
451 W. Wolff for insightful communications that inspired this work.

452 Declarations

- 453 • Competing interests: The author declares no competing interests.
- 454 • Data availability: The one-to-one correspondence between each glacial cycle
455 and the insolation-based interglacial spacing (Table S1) is provided in
456 `Data_S1_formula.xlsx` at <https://doi.org/10.5281/zenodo.19534114>. All the other
457 data used in this study are publicly available from the original sources cited in the
458 main text and Supplementary Information.

- 459 • Materials availability: Not applicable.
- 460 • Code availability: `PyleoClim`, used for wavelet-based spectral analysis, is available at
461 <https://pyleoclim-util.readthedocs.io/en/latest/> (last accessed 6 April 2026). Other
462 codes used in this study will be uploaded to a repository after the acceptance of the
463 paper.

464 References

- 465 [1] Clark, P. U., Shakun, J. D., Rosenthal, Y., Köhler, P. & Bartlein, P. J. Global
466 and regional temperature change over the past 4.5 million years. *Science* **383**,
467 884–890 (2024).
- 468 [2] Jouzel, J. *et al.* Orbital and millennial antarctic climate variability over the past
469 800,000 years. *science* **317**, 793–796 (2007).
- 470 [3] Rohling, E. J. *et al.* Comparison and synthesis of sea-level and deep-sea tem-
471 perature variations over the past 40 million years. *Reviews of Geophysics* **60**,
472 e2022RG000775 (2022).
- 473 [4] Lüthi, D. *et al.* High-resolution carbon dioxide concentration record 650,000–
474 800,000 years before present. *Nature* **453**, 379–382 (2008).
- 475 [5] Louergue, L. *et al.* Orbital and millennial-scale features of atmospheric ch4 over
476 the past 800,000 years. *Nature* **453**, 383–386 (2008).
- 477 [6] Lisiecki, L. E. & Raymo, M. E. A pliocene-pleistocene stack of 57 globally
478 distributed benthic $\delta^{18}\text{O}$ records. *Paleoceanography* **20** (2005).
- 479 [7] Herbert, T. D. The mid-pleistocene climate transition. *Annual Review of Earth*
480 *and Planetary Sciences* **51**, 389–418 (2023).
- 481 [8] Berends, C. J., Köhler, P., Lourens, L. J. & van de Wal, R. S. W. On the cause
482 of the mid-pleistocene transition. *Reviews of Geophysics* **59**, e2020RG000727
483 (2021). E2020RG000727 2020RG000727.
- 484 [9] McClymont, E. L., Sostdian, S. M., Rosell-Melé, A. & Rosenthal, Y. Pleistocene
485 sea-surface temperature evolution: Early cooling, delayed glacial intensifica-
486 tion, and implications for the mid-pleistocene climate transition. *Earth-Science*
487 *Reviews* **123**, 173–193 (2013).
- 488 [10] Laskar, J. *et al.* A long-term numerical solution for the insolation quantities of
489 the earth. *Astronomy & Astrophysics* **428**, 261–285 (2004).
- 490 [11] Milankovitch, M. Kanon der erdbestahlung und seine anwendung auf das
491 eiszeitproblem, 133. *Königlich Serbische Academie, Belgrade* (1941).

- 492 [12] Crucifix, M. Palinsol: insolation for palaeoclimate studies, r package version 0.93
493 (2016).
- 494 [13] Tzedakis, P., Crucifix, M., Mitsui, T. & Wolff, E. W. A simple rule to determine
495 which insolation cycles lead to interglacials. *Nature* **542**, 427–432 (2017).
- 496 [14] Paillard, D. Glacial cycles: toward a new paradigm. *Reviews of Geophysics* **39**,
497 325–346 (2001).
- 498 [15] Hays, J. D., Imbrie, J. & Shackleton, N. J. Variations in the earth’s orbit:
499 Pacemaker of the ice ages. *Science* **194**, 1121–1132 (1976).
- 500 [16] Berger, A. Support for the astronomical theory of climatic change. *Nature* **269**,
501 44–45 (1977).
- 502 [17] Raymo, M. The timing of major climate terminations. *Paleoceanography* **12**,
503 577–585 (1997).
- 504 [18] Ridgwell, A. J., Watson, A. J. & Raymo, M. E. Is the spectral signature of the
505 100 kyr glacial cycle consistent with a milankovitch origin? *Paleoceanography* **14**,
506 437–440 (1999).
- 507 [19] Blackburn, T., Kodama, S. & Piccione, G. Eccentricity paces late pleistocene
508 glaciations. *Geophysical Research Letters* **51**, e2024GL108751 (2024).
- 509 [20] Huybers, P. & Wunsch, C. Obliquity pacing of the late pleistocene glacial
510 terminations. *Nature* **434**, 491–494 (2005).
- 511 [21] Nyman, K. H. & Ditlevsen, P. D. The middle pleistocene transition by frequency
512 locking and slow ramping of internal period. *Climate Dynamics* **53**, 3023–3038
513 (2019).
- 514 [22] Bajo, P. *et al.* Persistent influence of obliquity on ice age terminations since the
515 middle pleistocene transition. *Science* **367**, 1235–1239 (2020).
- 516 [23] Abe-Ouchi, A. *et al.* Insolation-driven 100,000-year glacial cycles and hysteresis
517 of ice-sheet volume. *Nature* **500**, 190–193 (2013).
- 518 [24] Cheng, H. *et al.* The asian monsoon over the past 640,000 years and ice age
519 terminations. *nature* **534**, 640–646 (2016).
- 520 [25] Barker, S. *et al.* Persistent influence of precession on northern ice sheet variability
521 since the early pleistocene. *Science* **376**, 961–967 (2022).
- 522 [26] Hobart, B., Lisiecki, L. E., Rand, D., Lee, T. & Lawrence, C. E. Late pleistocene
523 100-kyr glacial cycles paced by precession forcing of summer insolation. *Nature*
524 *Geoscience* **16**, 717–722 (2023).

- 525 [27] Huybers, P. Combined obliquity and precession pacing of late pleistocene
526 deglaciations. *Nature* **480**, 229–232 (2011).
- 527 [28] Mitsui, T., Willeit, M. & Boers, N. Synchronization phenomena observed in
528 glacial-interglacial cycles simulated in an earth system model of intermediate
529 complexity. *Earth System Dynamics* **2023**, 1277–1294 (2023). URL <https://doi.org/10.5194/esd-14-1277-2023>.
530
- 531 [29] Mitsui, T., Tzedakis, P. C. & Wolff, E. W. Insolation evolution and ice volume
532 legacies determine interglacial and glacial intensity. *Climate of the Past* **18**,
533 1983–1996 (2022).
- 534 [30] Barker, S., Lisiecki, L. E., Knorr, G., Nuber, S. & Tzedakis, P. C. Distinct roles
535 for precession, obliquity, and eccentricity in pleistocene 100-kyr glacial cycles.
536 *Science* **387**, eadp3491 (2025).
- 537 [31] Foster, G. Time series analysis by projection. i. statistical properties of fourier
538 analysis. *Astronomical Journal v. 111, p. 541* **111**, 541 (1996).
- 539 [32] Kirchner, J. W. & Neal, C. Universal fractal scaling in stream chemistry and its
540 implications for solute transport and water quality trend detection. *Proceedings*
541 *of the National Academy of Sciences* **110**, 12213–12218 (2013).
- 542 [33] Khider, D. *et al.* Pyleoclim: Paleoclimate timeseries analysis and visualization
543 with python. *Paleoceanography and Paleoclimatology* **37**, e2022PA004509 (2022).
- 544 [34] Lisiecki, L. A benthic $\delta^{13}\text{C}$ -based proxy for atmospheric pCO_2 over the last 1.5
545 myr. *Geophysical Research Letters* **37** (2010).
- 546 [35] Zhou, Y., Lisiecki, L. E., Meyers, S. R., Lee, T. & Lawrence, C. Global and
547 regional pleistocene benthic $\delta^{18}\text{O}$ stacks with a comparison of different age
548 modeling strategies. *Geochronology* **8**, 85–107 (2026).
- 549 [36] Meyers, S. R. The evaluation of eccentricity-related amplitude modulation and
550 bundling in paleoclimate data: An inverse approach for astrochronologic testing
551 and time scale optimization. *Paleoceanography* **30**, 1625–1640 (2015).
- 552 [37] Huybers, P. Glacial variability over the last two million years: an extended depth-
553 derived age model, continuous obliquity pacing, and the pleistocene progression.
554 *Quaternary Science Reviews* **26**, 37–55 (2007).
- 555 [38] Mudelsee, M. & Stattegger, K. Exploring the structure of the mid-pleistocene
556 revolution with advanced methods of time-series analysis. *Geologische Rundschau*
557 **86**, 499–511 (1997).
- 558 [39] Clark, P. U. *et al.* The middle pleistocene transition: characteristics, mechanisms,
559 and implications for long-term changes in atmospheric pCO_2 . *Quaternary Science*

- 560 *Reviews* **25**, 3150–3184 (2006).
- 561 [40] Lisiecki, L. E. & Raymo, M. E. Plio–pleistocene climate evolution: trends and
562 transitions in glacial cycle dynamics. *Quaternary Science Reviews* **26**, 56–69
563 (2007).
- 564 [41] Huybers, P. & Wunsch, C. A depth-derived pleistocene age model: Uncertainty
565 estimates, sedimentation variability, and nonlinear climate change. *Paleoceanog-*
566 *raphy* **19** (2004).
- 567 [42] Huybers, P. & Aharonson, O. Orbital tuning, eccentricity, and the frequency
568 modulation of climatic precession. *Paleoceanography* **25** (2010).
- 569 [43] Liautaud, P. R., Hodell, D. A. & Huybers, P. J. Detection of significant climatic
570 precession variability in early pleistocene glacial cycles. *Earth and Planetary*
571 *Science Letters* **536**, 116137 (2020).
- 572 [44] Watanabe, Y. *et al.* Astronomical forcing shaped the timing of early pleistocene
573 glacial cycles. *Communications Earth & Environment* **4** (2023).
- 574 [45] Liebrand, D. & de Bakker, A. Bispectra of climate cycles show how ice ages are
575 fuelled. *Climate of the Past* **15**, 1959–1983 (2019).
- 576 [46] Bolton, E. W., Maasch, K. A. & Lilly, J. M. A wavelet analysis of plio-pleistocene
577 climate indicators: A new view of periodicity evolution. *Geophysical Research*
578 *Letters* **22**, 2753–2756 (1995).
- 579 [47] Rial, J. A. Pacemaking the ice ages by frequency modulation of earth’s orbital
580 eccentricity. *Science* **285**, 564–568 (1999).
- 581 [48] Cheng, H. *et al.* Ice age terminations. *Science* **326**, 248–252 (2009).
- 582 [49] Raymo, M. E. & Nisancioglu, K. H. The 41 kyr world: Milankovitch’s other
583 unsolved mystery. *Paleoceanography* **18** (2003).
- 584 [50] Legrain, E., Parrenin, F. & Capron, E. A gradual change is more likely to have
585 caused the mid-pleistocene transition than an abrupt event. *Communications*
586 *Earth & Environment* **4**, 90 (2023).
- 587 [51] Kodama, S. T. & Blackburn, T. Eccentricity controls the magnitude and peri-
588 odicity of pleistocene glacial cycles. *Paleoceanography and Paleoclimatology* **41**,
589 e2026PA005420 (2026).
- 590 [52] Hönlisch, B., Hemming, N. G., Archer, D., Siddall, M. & McManus, J. F.
591 Atmospheric carbon dioxide concentration across the mid-pleistocene transition.
592 *Science* **324**, 1551–1554 (2009).

- 593 [53] Chalk, T. B. *et al.* Causes of ice age intensification across the mid-pleistocene
594 transition. *Proceedings of the National Academy of Sciences* **114**, 13114–13119
595 (2017).
- 596 [54] Willeit, M., Ganopolski, A., Calov, R. & Brovkin, V. Mid-pleistocene transition in
597 glacial cycles explained by declining co2 and regolith removal. *Science Advances*
598 **5**, eaav7337 (2019).
- 599 [55] Yehudai, M. *et al.* Evidence for a northern hemispheric trigger of the 100,000-
600 y glacial cyclicity. *Proceedings of the National Academy of Sciences* **118**,
601 e2020260118 (2021).
- 602 [56] Clark, P. U. & Pollard, D. Origin of the middle pleistocene transition by ice sheet
603 erosion of regolith. *Paleoceanography* **13**, 1–9 (1998).
- 604 [57] An, Z. *et al.* Mid-pleistocene climate transition triggered by antarctic ice sheet
605 growth. *science* **385**, 560–565 (2024).
- 606 [58] Basak, C. *et al.* Southern hemisphere initiation of the mid-pleistocene transition.
607 *Science Advances* **12**, eaea6811 (2026).
- 608 [59] Hines, S. K. *et al.* Revisiting the mid-pleistocene transition ocean circulation
609 crisis. *Science* **386**, 681–686 (2024).
- 610 [60] Mitsui, T., Ditlevsen, P., Boers, N. & Crucifix, M. 100 kyr ice age cycles as a
611 timescale-matching problem. *Earth System Dynamics* **16**, 1569–1584 (2025).
- 612 [61] Lisiecki, L. E. Links between eccentricity forcing and the 100,000-year glacial
613 cycle. *Nature geoscience* **3**, 349–352 (2010).
- 614 [62] Meyers, S. R. Cyclostratigraphy and the problem of astrochronologic testing.
615 *Earth-Science Reviews* **190**, 190–223 (2019).
- 616 [63] Bloomfield, P. *Fourier analysis of time series: an introduction* (John Wiley &
617 Sons, 2004).
- 618 [64] Thomson, D. J. Spectrum estimation and harmonic analysis. *Proceedings of the*
619 *IEEE* **70**, 1055–1096 (1982).
- 620 [65] Schulz, M. & Mudelsee, M. Redfit: estimating red-noise spectra directly from
621 unevenly spaced paleoclimatic time series. *Computers & Geosciences* **28**, 421–426
622 (2002).
- 623 [66] Lomb, N. R. Least-squares frequency analysis of unequally spaced data.
624 *Astrophysics and space science* **39**, 447–462 (1976).
- 625 [67] Scargle, J. D. Studies in astronomical time series analysis. ii-statistical aspects
626 of spectral analysis of unevenly spaced data. *Astrophysical Journal, Part 1, vol.*

- 627 *263*, Dec. 15, 1982, p. 835-853. **263**, 835–853 (1982).
- 628 [68] Wu, Z., Huang, N. E., Long, S. R. & Peng, C.-K. On the trend, detrending, and
629 variability of nonlinear and nonstationary time series. *Proceedings of the National*
630 *Academy of Sciences* **104**, 14889–14894 (2007).
- 631 [69] Zhu, F. *et al.* Climate models can correctly simulate the continuum of global-
632 average temperature variability. *Proceedings of the National Academy of Sciences*
633 **116**, 8728–8733 (2019).

1 Supplementary Information for Beyond the
2 100-kyr and 41-kyr dichotomy: ~ 76 -kyr and
3 ~ 52 -kyr signals and forbidden periodicities

4 Takahito Mitsui

5 Faculty of Health Data Science, Juntendo University, Urayasu, Chiba,
6 279-0013, Japan.

7
8 Contact: takahito321@gmail.com.

9 **Contents**

- 10 • Supplementary Notes
11 • References
12 • Supplementary Figures S1–S18
13 • Supplementary Table S1, which is also available as
14 Data_S1_formula.xlsx at <https://doi.org/10.5281/zenodo.19534114>

15 **Derivation of the approximation formulae of**
16 **interglacial spacings**

17 Following Tzedakis et al. (2017) [1], we assume that each interglacial onset can be
18 linked with a specific peak in the caloric summer half-year insolation at 65°N [2, 3].
19 Thus, the insolation-based interglacial spacings (T_{ins}) are defined between successive
20 caloric summer half-year insolation peaks that finally induced each interglacial [1]
21 (Figs. S11a–S13a). Here we derive approximate formulae for T_{ins} of each glacial cycle
22 based on local information on climatic precession and obliquity [4] (Fig. S15–S18).

23 It is known that the caloric summer half-year insolation, especially at 65°N, is well
24 approximated by a superposition of standardized indices of climatic precession and
25 obliquity [2, 5]. Since the climatic precession oscillates more rapidly than obliquity, the
26 insolation peak closest to the deglaciation isotopic change is more tightly linked with
27 a climatic precession peak (minimum). Indeed, the link between the length of glacial

28 cycles and the durations of astronomical cycles—particularly precession—has been
 29 noted in various studies [6–9]. On the other hand, the duration of climatic precession
 30 cycles varies widely (between 14 and 31 kyr) when eccentricity is low, whereas it
 31 remains relatively stable around 22.1 kyr when eccentricity is high (Fig. S14) [9, 10].
 32 Building on this, we here derive finer relationships between T_{ins} and the evolving
 33 durations of precession and obliquity cycles.

34 For each glacial cycle, we approximate the local variations in the caloric summer
 35 half-year insolation as $f(t) = A_p \cos(\omega_p t + \varphi_p) + A_o \cos(\omega_o t + \varphi_o)$, accounting for the
 36 respective positive contributions of climatic precession and obliquity to the insolation.
 37 Here, $A_{p,o}$ are the local-mean amplitudes, $\omega_{p,o}$ are the angular frequencies (correspond-
 38 ing to local-mean periods $T_{p,o}$), and $\varphi_{p,o}$ are the local phases of climatic precession and
 39 obliquity cycles. Note that the maxima of $A_p \cos(\omega_p t + \varphi_p)$ correspond to the minima
 40 of the climatic precession cycles, as precession minima contribute to maximal insola-
 41 tion. Then, we can derive analytical expressions for T_{ins} . A complete correspondence
 42 between individual glacial cycles and their respective formulae is provided in Table S1.

Formula type 2a, 3a, 4a and 5a. When the peaks of climatic precession and
 obliquity nearly coincide and collectively induce an interglacial, we define this peak
 time as $t = 0$ by setting $\varphi_p = \varphi_o = 0$ (Fig. S19a). If the spacing T_{ins} between the peak
 at $t = 0$ and a subsequent interglacial-inducing peak is close to the n -th multiple of the
 local-mean precession period T_p , it can be expressed as $T_{\text{ins}} = nT_p + \delta$, where the small
 shift δ reflects the phase modulation by obliquity. By linearizing the peak condition
 $f'(nT_p + \delta) = 0$ as $f'(nT_p + \delta) \approx f'(nT_p) + f''(nT_p)\delta = 0$, we obtain approximation
 formulae for T_{ins} ($n = 2, 3, 4, 5$), called type-a:

$$T_{\text{ins}} \approx nT_p - \frac{A_o \omega_o \sin(n\omega_o T_p)}{A_p \omega_p^2 + A_o \omega_o^2 \cos(n\omega_o T_p)}.$$

43 An example of type-a is the ~ 76 -kyr spacing between interglacials MIS 11c and MIS 9e
 44 (Fig. S15), where the corresponding insolation peaks are separated by approximately
 45 four precession cycles ($n = 4$), and the local-mean precession period is $T_p = 18.25$ kyr.
 46 Furthermore, the local-mean obliquity period is $T_o = 41.5$ kyr. The type-a formula
 47 then predicts $T_{\text{ins}} = 74.3$ kyr. This value is closer to the actual value of 76 kyr than the
 48 simple multiple of precession, $nT_p = 73$ kyr, obtained without the shift $\delta = 1.43$ kyr.

Formulae type 1b and 3b. The second case occurs when a glacial cycle spans
 roughly one or three precession cycles (i.e., $n = 1$ or 3), with the insolation locally
 approximated as $f(t) = -A_p \cos(\omega_p t) - A_o \cos(\omega_o t)$ over the interval $-\frac{n}{2}T_p \lesssim t \lesssim \frac{n}{2}T_p$
 (corresponding to $\varphi_p = \varphi_o = \pi$). For this case, we assume that deglaciations occur at
 $t = \pm(\frac{n}{2}T_p + \delta)$, with δ being a small obliquity-induced shift. By linearizing the peak
 condition $f'(\frac{n}{2}T_p + \delta) \approx f'(\frac{n}{2}T_p) + f''(\frac{n}{2}T_p)\delta = 0$, we obtain approximation formulae
 for T_{ins} ($n = 1, 3$), called type-1b or 3b:

$$T_{\text{ins}} \approx nT_p + \frac{2A_o \omega_o \sin(\frac{n}{2}\omega_o T_p)}{A_p \omega_p^2 - A_o \omega_o^2 \cos(\frac{n}{2}\omega_o T_p)}.$$

49 An example of type-3b is the spacing between interglacials MIS 37 and MIS 35
50 (Fig. S16). The corresponding insolation peaks are separated by approximately three
51 precession cycles ($n = 3$), and the local-mean precession period is $T_p = 19$ kyr. Fur-
52 thermore, the local-mean obliquity period is $T_o = 39$ kyr. Then, the type-3b formula
53 predicts $T_{\text{ins}} = 54.2$ kyr. This value is closer to the actual value of 53 kyr than the
54 simple multiple of precession, $nT_p = 57$ kyr, obtained without the shift $\delta = -2.8$ kyr.

Formulae type 2b. Consider a case where a glacial cycle spans approximately two precession cycles, in which the central precession peak is counteracted by an obliquity minimum, while the outer precession peaks are enhanced by adjacent obliquity maxima. This situation is approximated as $f(t) = A_p \cos(\omega_p t) - A_o \cos(\omega_o t)$ over the interval $-T_p \lesssim t \lesssim T_p$ (corresponding to $\varphi_p = 0$ and $\varphi_o = \pi$). In a similar manner to the derivation of the formulae type-1b and 3b, T_{ins} is given by formula called type-2b:

$$T_{\text{ins}} \approx 2T_p + \frac{2A_o\omega_o \sin(\omega_o T_p)}{A_p\omega_p^2 - A_o\omega_o^2 \cos(\omega_o T_p)}.$$

Formulae type 4b. Consider a case where a glacial cycle spans approximately four precession cycles, in which the central precession peak is enhanced by an obliquity maximum, while the outer precession peaks are also enhanced by adjacent obliquity maxima. This situation is approximated as $f(t) = A_p \cos(\omega_p t) + A_o \cos(\omega_o t)$ over the interval $-2T_p \lesssim t \lesssim 2T_p$ (corresponding to $\varphi_p = \varphi_o = 0$). In a similar manner to the derivation of the formulae type-2b, T_{ins} is given by formula called type-4b:

$$T_{\text{ins}} \approx 4T_p - \frac{2A_o\omega_o \sin(2\omega_o T_p)}{A_p\omega_p^2 + A_o\omega_o^2 \cos(2\omega_o T_p)}.$$

Formulae type 1c and 2c. Consider a case where a glacial cycle spans roughly one or two precession cycles ($n = 1$ or 2), with the insolation locally approximated as $f(t) = A_p \cos(\omega_p t) - A_o \sin(\omega_o t)$ over the interval $0 \leq t \lesssim nT_p$ (corresponding to $\varphi_p = 0$ and $\varphi_o = \frac{\pi}{2}$). In this case, the deglaciations occur at $t = 0$ and $t = nT_p + \delta$, where δ is a small shift. By linearizing the peak condition $f'(nT_p + \delta) \approx f'(nT_p) + f''(nT_p)\delta = 0$, we obtain approximation formulae for T_{ins} ($n = 1, 2$), called type-1c or 2c:

$$T_{\text{ins}} \approx nT_p - \frac{A_o\omega_o \cos(n\omega_o T_p)}{A_p\omega_p^2 - A_o\omega_o^2 \sin(n\omega_o T_p)}.$$

Formula 2d. Consider a case where a glacial cycle spans roughly two precession cycles, with the insolation locally approximated as $f(t) = A_p \cos(\omega_p t) + A_o \sin(\omega_o t)$ over the interval $0 \leq t \lesssim 2T_p$ (corresponding to $\varphi_p = 0$ and $\varphi_o = -\frac{\pi}{2}$). In this case, the deglaciations occur at $t = 0$ and $t = 2T_p + \delta$, where δ is a small shift. By linearizing the peak condition $f'(2T_p + \delta) \approx f'(2T_p) + f''(2T_p)\delta = 0$, we obtain the approximation formula for T_{ins} , called type-2d:

$$T_{\text{ins}} \approx 2T_p + \frac{A_o\omega_o \cos(2\omega_o T_p)}{A_p\omega_p^2 - A_o\omega_o^2 \sin(2\omega_o T_p)}.$$

Formula type pp. In this case, the interglacial spacing is primarily determined by the spacing between precession peaks; while obliquity cycles may shift the timing of both deglaciations, they do so by the same amount, leaving the net spacing almost unchanged. Therefore,

$$T_{\text{ins}} \approx nT_p.$$

55 **Choice of amplitude $A_{p,o}$.** Climatic precession and obliquity contribute nearly
56 equally to the total variance in the caloric summer half-year insolation at 65°N [2, 3].
57 Therefore, for simplicity, we set $A_{p,o} = 1$ for 65°N caloric summer half-year insolation
58 except for the following two cycles. However, the cycle from MIS 99 to 97 as well as
59 the cycle from MIS 97 to 95 are characterized by low eccentricity (i.e., low precession
60 amplitude) and high obliquity amplitude. Assessing their variances locally, we took
61 $A_o/A_p = 3$ and $A_o/A_p = 2.5$ for the former and the latter, respectively.

62 **Two exceptions** The spacings MIS 95–93 and MIS 93–91 represent epochs during
63 which eccentricity remains near zero. The aforementioned formulae are inapplicable to
64 these events because deglaciation coincides with the obliquity maximum at 2386 ka,
65 where eccentricity is virtually zero. For these cases, we adopt simplified estimates for
66 T_{ins} . The MIS 95–93 interval is assumed to be initiated by an insolation peak occurring
67 midway between the obliquity maximum at 2426 ka and the precession minimum at
68 2419 ka, and is finalized by the obliquity maximum at 2386 ka. Consequently, the
69 spacing is estimated as $(2426 + 2419)/2 - 2386 = 36.5$ kyr. Similarly, the MIS 93–91
70 interval is initiated by the 2386-ka obliquity maximum and finalized by an insolation
71 peak midway between the obliquity maximum at 2348 ka and the precession minimum
72 at 2347 ka. The spacing is thus estimated as $2386 - (2348 + 2347)/2 = 38.5$ kyr.

73 References

- 74 [1] Tzedakis, P., Crucifix, M., Mitsui, T. & Wolff, E. W. A simple rule to determine
75 which insolation cycles lead to interglacials. *Nature* **542**, 427–432 (2017).
- 76 [2] Milankovitch, M. Kanon der erdbestahlung und seine anwendung auf das
77 eiszeitproblem, 133. *Königlich Serbische Academie, Belgrade* (1941).
- 78 [3] Crucifix, M. Palinsol: insolation for palaeoclimate studies, r package version 0.93
79 (2016).
- 80 [4] Laskar, J. *et al.* A long-term numerical solution for the insolation quantities of
81 the earth. *Astronomy & Astrophysics* **428**, 261–285 (2004).
- 82 [5] Nisancioglu, K. H. Plio-pleistocene glacial cycles and milankovitch variability.
83 *Elements of Physical Oceanography: A derivative of the Encyclopedia of Ocean*
84 *Sciences* 344 (2009).
- 85 [6] Abe-Ouchi, A. *et al.* Insolation-driven 100,000-year glacial cycles and hysteresis
86 of ice-sheet volume. *Nature* **500**, 190–193 (2013).

- 87 [7] Cheng, H. *et al.* The asian monsoon over the past 640,000 years and ice age
88 terminations. *nature* **534**, 640–646 (2016).
- 89 [8] Hobart, B., Lisiecki, L. E., Rand, D., Lee, T. & Lawrence, C. E. Late pleistocene
90 100-kyr glacial cycles paced by precession forcing of summer insolation. *Nature*
91 *Geoscience* **16**, 717–722 (2023).
- 92 [9] Blackburn, T., Kodama, S. & Piccione, G. Eccentricity paces late pleistocene
93 glaciations. *Geophysical Research Letters* **51**, e2024GL108751 (2024).
- 94 [10] Huybers, P. & Aharonson, O. Orbital tuning, eccentricity, and the frequency
95 modulation of climatic precession. *Paleoceanography* **25** (2010).
- 96 [11] Lisiecki, L. E. & Raymo, M. E. A pliocene-pleistocene stack of 57 globally
97 distributed benthic $\delta^{18}\text{O}$ records. *Paleoceanography* **20** (2005).
- 98 [12] Lisiecki, L. A benthic $\delta^{13}\text{C}$ -based proxy for atmospheric pCO_2 over the last 1.5
99 myr. *Geophysical Research Letters* **37** (2010).
- 100 [13] Zhou, Y., Lisiecki, L. E., Meyers, S. R., Lee, T. & Lawrence, C. Global and
101 regional pleistocene benthic $\delta^{18}\text{O}$ stacks with a comparison of different age
102 modeling strategies. *Geochronology* **8**, 85–107 (2026).
- 103 [14] Meyers, S. R. The evaluation of eccentricity-related amplitude modulation and
104 bundling in paleoclimate data: An inverse approach for astrochronologic testing
105 and time scale optimization. *Paleoceanography* **30**, 1625–1640 (2015).
- 106 [15] Meyers, S. R. Cyclostratigraphy and the problem of astrochronologic testing.
107 *Earth-Science Reviews* **190**, 190–223 (2019).
- 108 [16] Huybers, P. Glacial variability over the last two million years: an extended depth-
109 derived agetmodel, continuous obliquity pacing, and the pleistocene progression.
110 *Quaternary Science Reviews* **26**, 37–55 (2007).
- 111 [17] Barker, S. *et al.* Persistent influence of precession on northern ice sheet variability
112 since the early pleistocene. *Science* **376**, 961–967 (2022).
- 113 [18] Khider, D. *et al.* Pyleoclim: Paleoclimate timeseries analysis and visualization
114 with python. *Paleoceanography and Paleoclimatology* **37**, e2022PA004509 (2022).

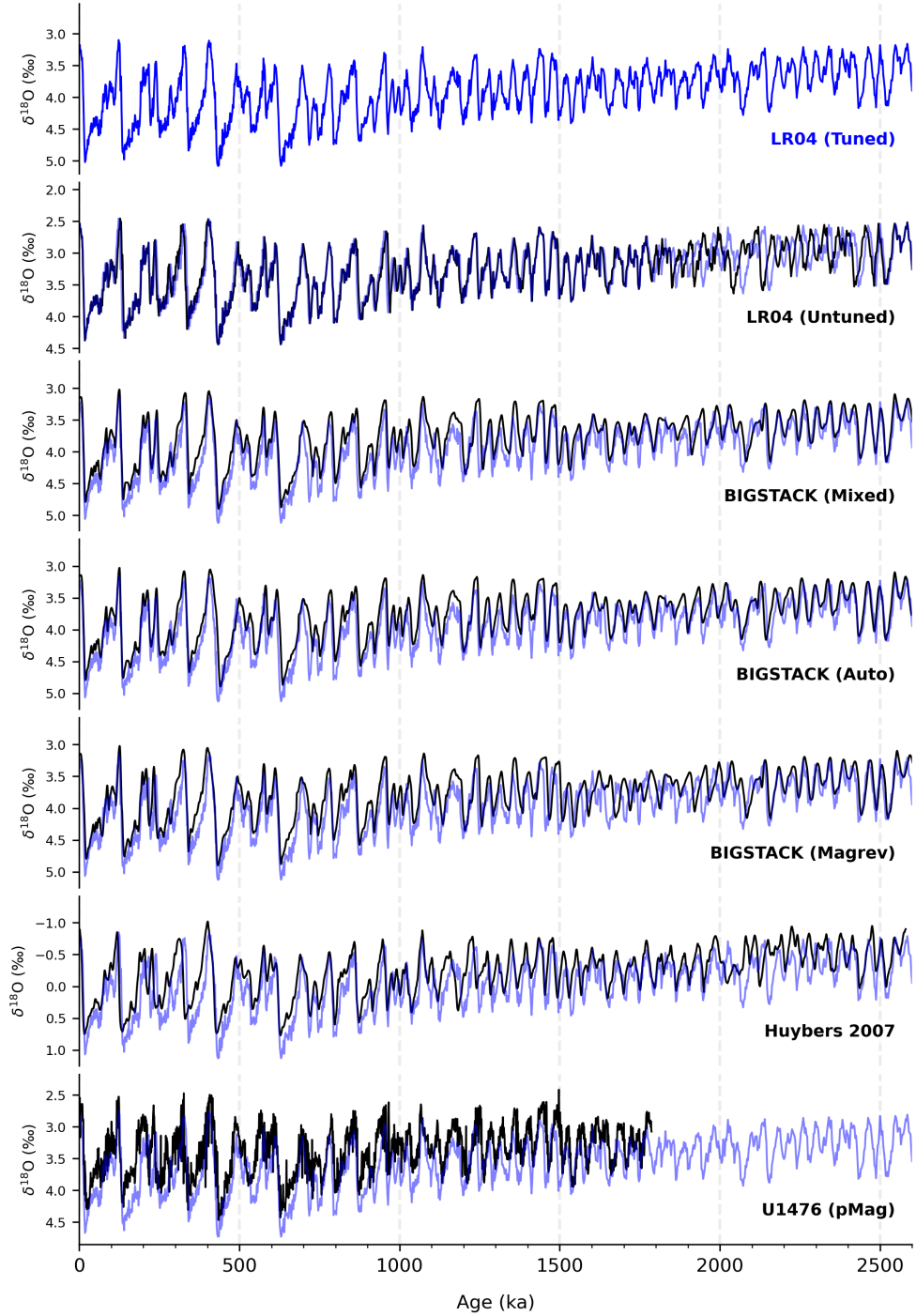


Fig. S1 Benthic $\delta^{18}\text{O}$ stacks and an individual record analyzed in this study. (a) The LR04 tuned stack [11]. In the subsequent panels, the LR04 stack is shown as a blue background reference, vertically shifted to match the mean $\delta^{18}\text{O}$ value of each target record (black). (b) The tuning-free version of the LR04 stack from Lisiecki (2010) [12]. (c) The $\text{BIGSTACK}_{\text{mixed}}$ record using speleothem-based age constraints for 0–654 ka and ice-sheet model tuning for earlier intervals [13]. (d) The $\text{BIGSTACK}_{\text{auto}}$ record obtained from $\text{BIGSTACK}_{\text{magrev}}$ (below) by applying the eTimeOpt algorithm [14, 15] to minimally tune the pervasive 41-kyr obliquity signal. (e) The $\text{BIGSTACK}_{\text{magrev}}$ record constrained by paleomagnetic events over the last 2.606 Ma to minimize orbital circularity. (f) The depth-derived stack of Huybers (2007) [16]. (g) The single-site benthic $\delta^{18}\text{O}$ record from IODP Site U1476, anchored to an independent paleomagnetic age model (U1476pMag) [17]. This record spans only the last 1786.542 kyr.

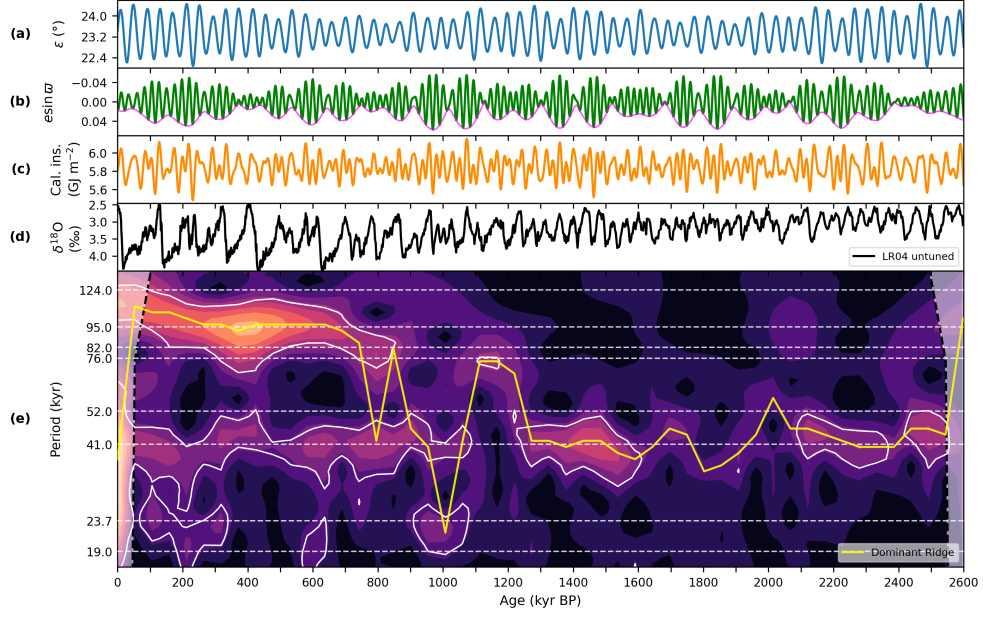


Fig. S2 Time-series and wavelet analyses of the LR04 benthic $\delta^{18}\text{O}$ stack record free from orbital tuning [12], aligned with astronomical forcing [4] over the last 2.6 Myr. (a) Obliquity (ϵ). (b) Climatic precession ($e \sin \varpi$, green) shown with its eccentricity envelope (e , magenta). (c) Caloric summer half-year insolation at 65°N [2, 3]. (d) LR04 benthic $\delta^{18}\text{O}$ stack record without orbital tuning. [12] (e) Wavelet power scalogram of the $\delta^{18}\text{O}$ record. The yellow line indicates the ridge of maximum wavelet power. Areas enclosed by white dashed lines indicate power significant at the 95% confidence level against an AR(1) benchmark. Horizontal dashed lines denote major astronomical periodicities, including the 76-kyr and 52-kyr scales discussed in this study.

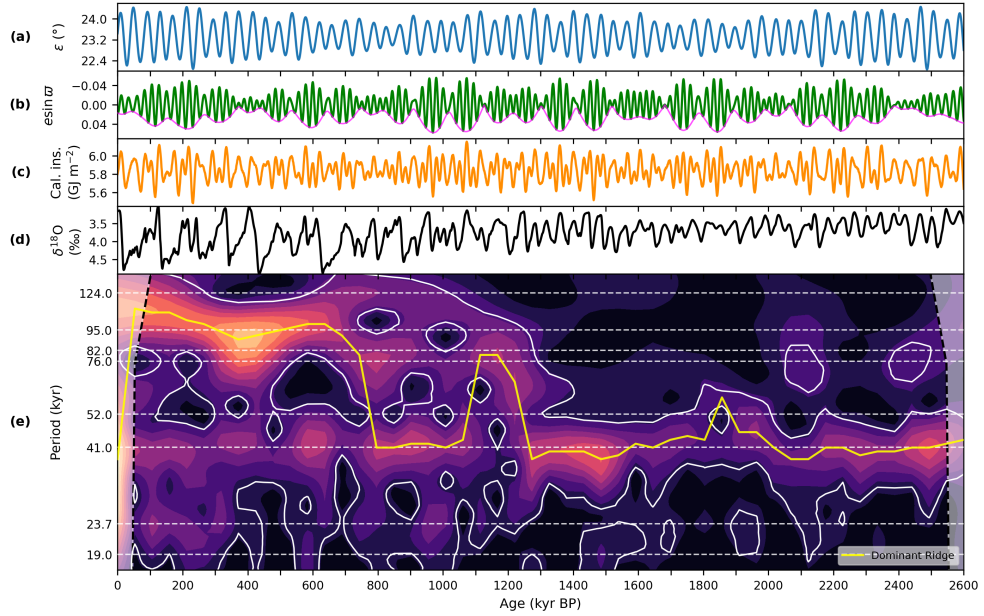


Fig. S3 Time-series and wavelet analyses of the benthic $\delta^{18}\text{O}$ stack record of $\text{BIGSTACK}_{\text{mixed}}$ [13], aligned with astronomical forcing [4] over the last 2.6 Myr. (a) Obliquity (ϵ). (b) Climatic precession ($e \sin \varpi$, green) shown with its eccentricity envelope (e , magenta). (c) Caloric summer half-year insolation at 65°N [2, 3]. (d) The benthic $\delta^{18}\text{O}$ stack record of Huybers (2007) [16]. (e) Wavelet power scalogram of the $\delta^{18}\text{O}$ record. The yellow line indicates the ridge of maximum wavelet power. Areas enclosed by white dashed lines indicate power significant at the 95% confidence level against an AR(1) benchmark. Horizontal dashed lines denote major astronomical periodicities, including the 76-kyr and 52-kyr scales discussed in this study.

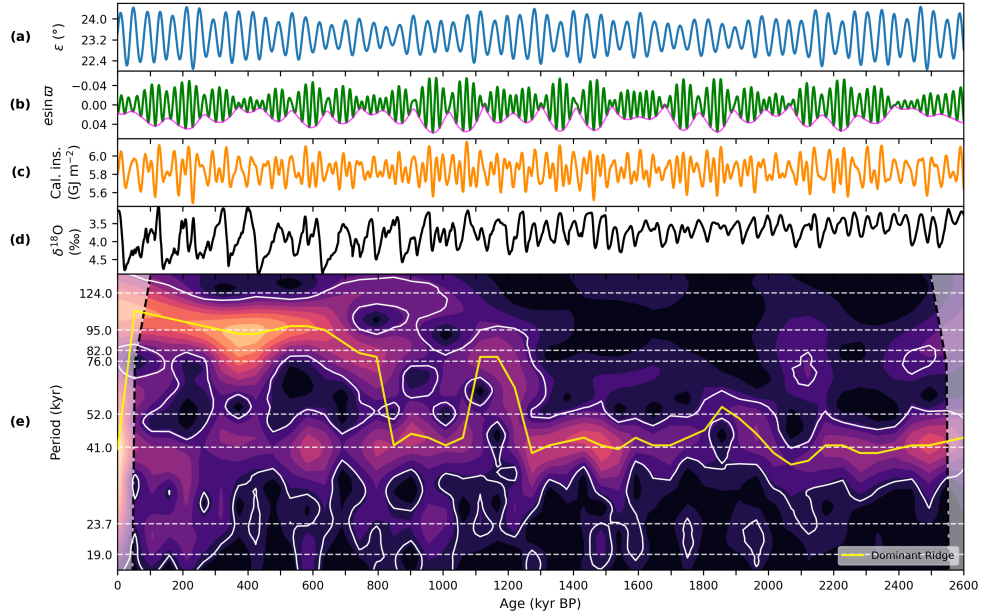


Fig. S4 Time-series and wavelet analyses of the benthic $\delta^{18}\text{O}$ stack record of BIGSTACK_{magrev} [13], aligned with astronomical forcing [4] over the last 2.6 Myr. (a) Obliquity (ϵ). (b) Climatic precession ($e \sin \omega$, green) shown with its eccentricity envelope (e , magenta). (c) Caloric summer half-year insolation at 65°N [2, 3]. (d) The benthic $\delta^{18}\text{O}$ stack record of Huybers (2007) [16]. (e) Wavelet power scalogram of the $\delta^{18}\text{O}$ record. The yellow line indicates the ridge of maximum wavelet power. Areas enclosed by white dashed lines indicate power significant at the 95% confidence level against an AR(1) benchmark. Horizontal dashed lines denote major astronomical periodicities, including the 76-kyr and 52-kyr scales discussed in this study.

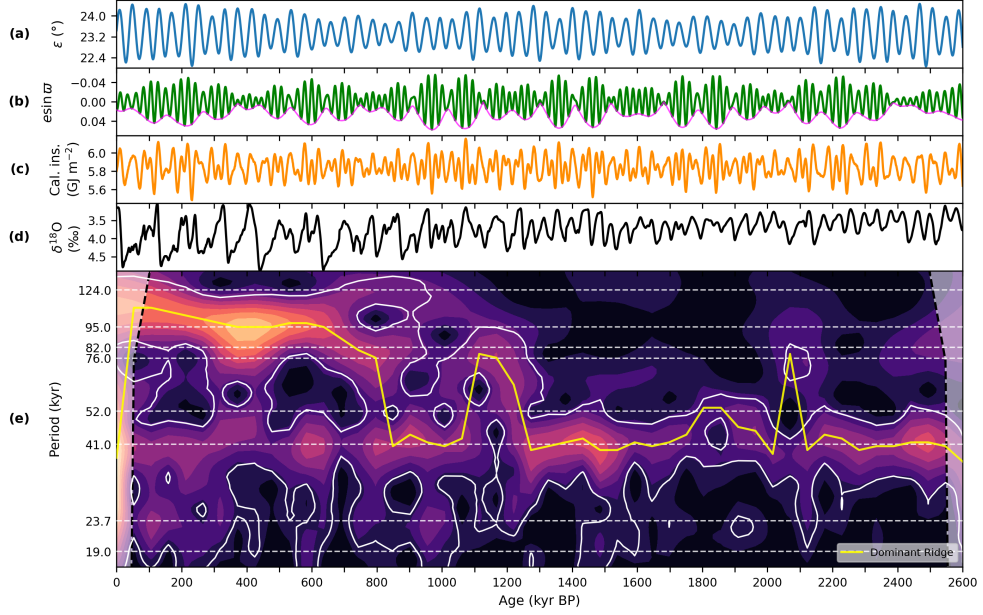


Fig. S5 Time-series and wavelet analyses of the benthic $\delta^{18}\text{O}$ stack record of $\text{BIGSTACK}_{\text{auto}}$ [13], aligned with astronomical forcing [4] over the last 2.6 Myr. (a) Obliquity (ϵ). (b) Climatic precession ($e \sin \omega$, green) shown with its eccentricity envelope (e , magenta). (c) Caloric summer half-year insolation at 65°N [2, 3]. (d) The benthic $\delta^{18}\text{O}$ stack record of Huybers (2007) [16]. (e) Wavelet power scalogram of the $\delta^{18}\text{O}$ record. The yellow line indicates the ridge of maximum wavelet power. Areas enclosed by white dashed lines indicate power significant at the 95% confidence level against an AR(1) benchmark. Horizontal dashed lines denote major astronomical periodicities, including the 76-kyr and 52-kyr scales discussed in this study.

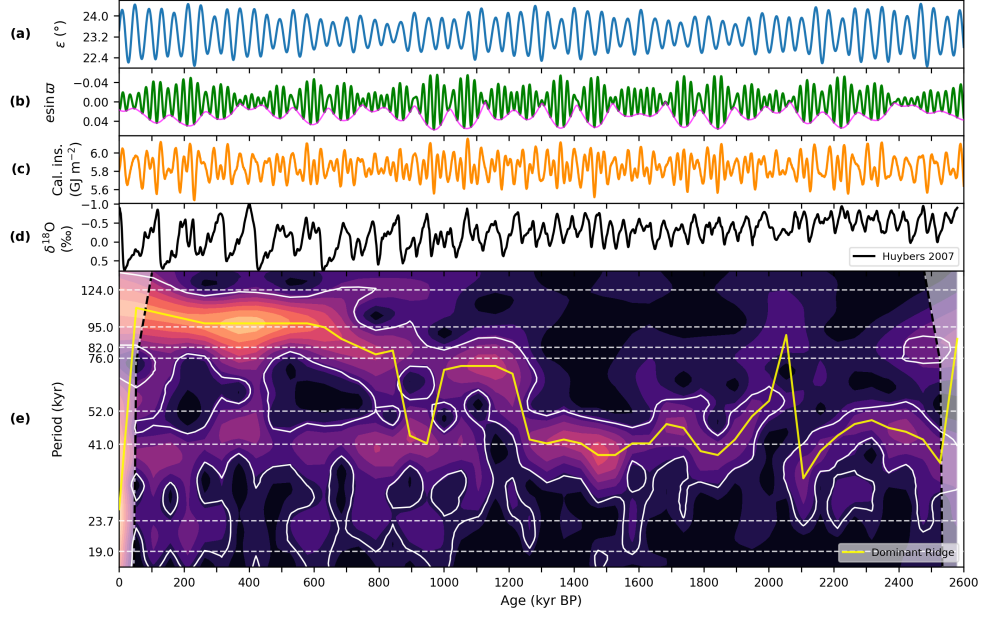


Fig. S6 Time-series and wavelet analyses of the benthic $\delta^{18}\text{O}$ stack record of Huybers (2007) [16], aligned with astronomical forcing [4] over the last 2.6 Myr. (a) Obliquity (ϵ). (b) Climatic precession ($e \sin \omega$, green) shown with its eccentricity envelope (e , magenta). (c) Caloric summer half-year insolation at 65°N [2, 3]. (d) The benthic $\delta^{18}\text{O}$ stack record of Huybers (2007) [16]. (e) Wavelet power scalogram of the $\delta^{18}\text{O}$ record. The yellow line indicates the ridge of maximum wavelet power. Areas enclosed by white dashed lines indicate power significant at the 95% confidence level against an AR(1) benchmark. Horizontal dashed lines denote major astronomical periodicities, including the 76-kyr and 52-kyr scales discussed in this study.

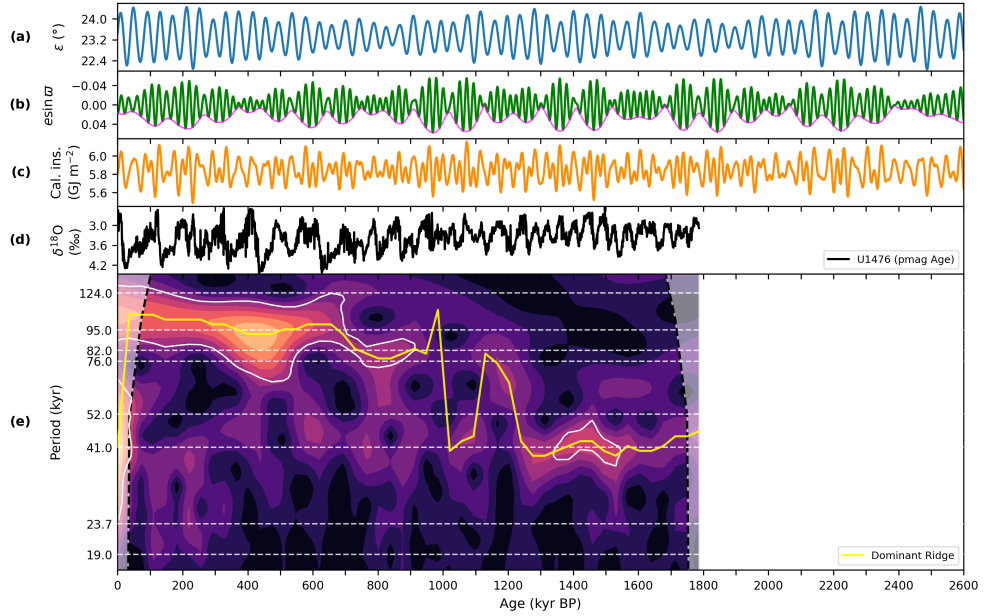


Fig. S7 Time-series and wavelet analyses of the benthic $\delta^{18}\text{O}$ record from U1476pMag [17], aligned with astronomical forcing [4] over the last 2.6 Myr. (a) Obliquity (ϵ). (b) Climatic precession ($e \sin \omega$, green) shown with its eccentricity envelope (e , magenta). (c) Caloric summer half-year insolation at 65°N [2, 3]. (d) The benthic $\delta^{18}\text{O}$ record from U1476pMag [17]. (e) Wavelet power scalogram of the $\delta^{18}\text{O}$ record. The yellow line indicates the ridge of maximum wavelet power. Areas enclosed by white dashed lines indicate power significant at the 95% confidence level against an AR(1) benchmark. Horizontal dashed lines denote major astronomical periodicities, including the 76-kyr and 52-kyr scales discussed in this study.

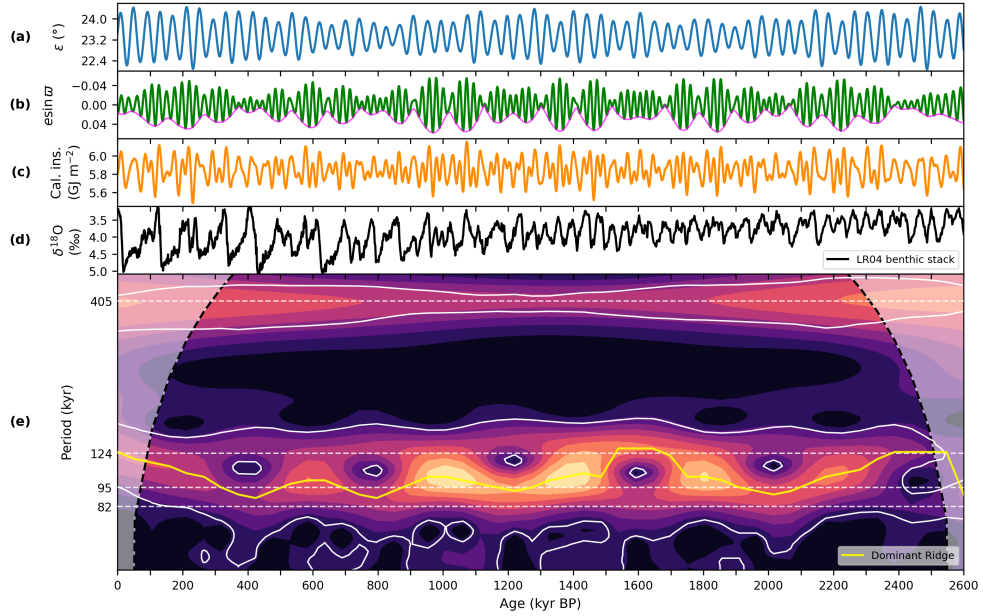


Fig. S8 Time-series and wavelet analyses of eccentricity, aligned with other astronomical elements [4] and the LR04 benthic $\delta^{18}\text{O}$ stack record over the last 2.6 Myr. (a) Obliquity (ϵ). (b) Climatic precession ($e \sin \varpi$, green) shown with its eccentricity envelope (e , magenta). (c) Caloric summer half-year insolation at 65°N [2, 3]. (d) LR04 benthic $\delta^{18}\text{O}$ stack record without orbital tuning. [12] (e) Wavelet power scalogram of eccentricity. The yellow line indicates the ridge of maximum wavelet power obtained by omitting the 405-kyr band. Areas enclosed by white dashed lines indicate power significant at the 95% confidence level against an AR(1) benchmark. Horizontal dashed lines denote major astronomical periodicities of eccentricity.

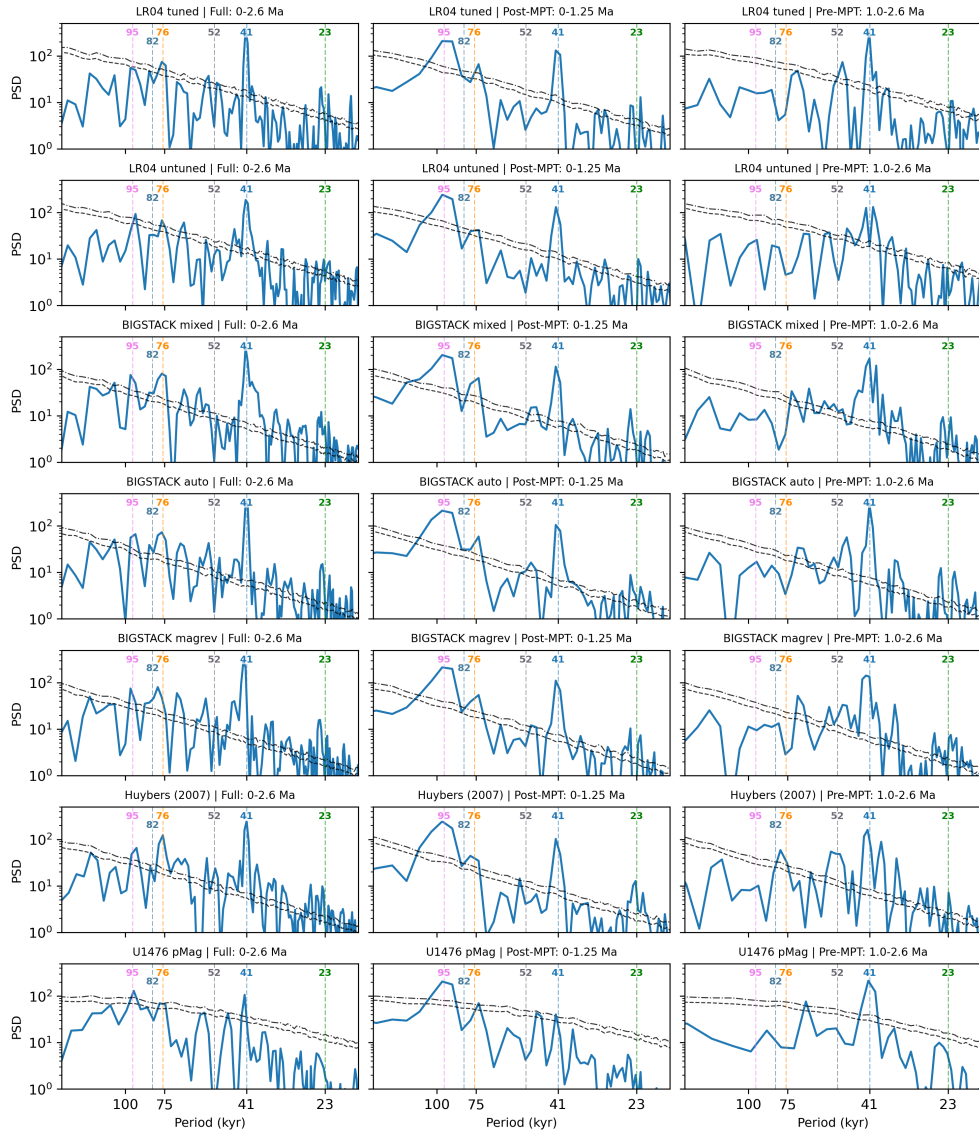


Fig. S9 Comparison of conventional periodograms across multiple benthic $\delta^{18}\text{O}$ records in Supplementary Information Fig. 1. Each column represents a specific time interval: the entire Quaternary (0–2.6 Ma; left), the mid-to-late Pleistocene (0–1.25 Ma; center), and the early Pleistocene (1.0–2.6 Ma; right). Blue lines indicate the PSD of the standardized $\delta^{18}\text{O}$ records, while dashed and dotted black lines denote the 95% and 90% confidence levels, respectively, against an AR(1) benchmark. Vertical dashed lines highlight key periodicities: the canonical eccentricity (95 kyr), obliquity (41 kyr), and precession (23 kyr) cycles, as well as the sub-harmonics analyzed in this study (82, 76, and 52 kyr). The time series is interpolated at 1-kyr intervals before the analysis and then linearly detrended over the analysis period. All analyses are performed using the `pyleoclim` (version 1.2.0) [18].

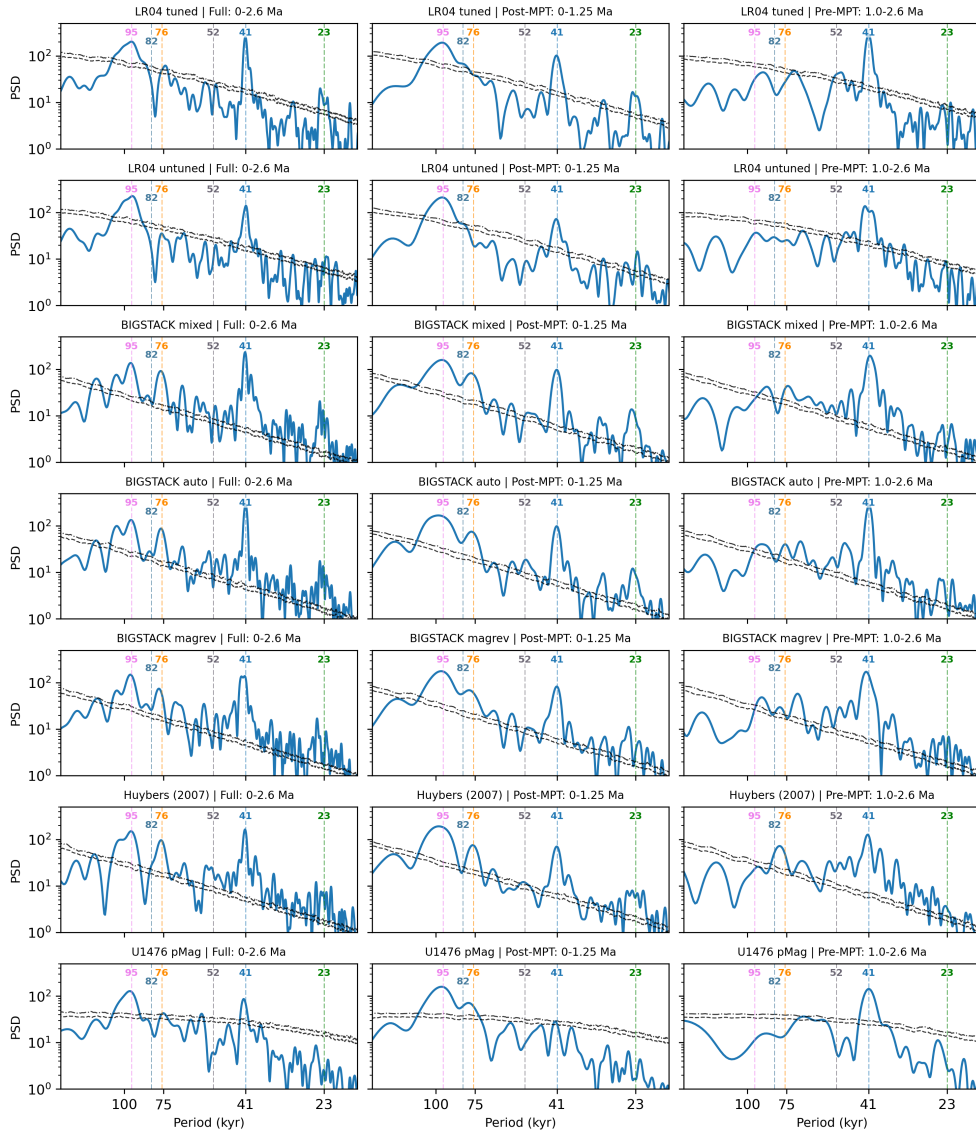


Fig. S10 Comparison of Lomb-Scargle spectra across multiple benthic $\delta^{18}\text{O}$ records in Supplementary Information Fig. 1. Each column represents a specific time interval: the entire Quaternary (0–2.6 Ma; left), the mid-to-late Pleistocene (0–1.25 Ma; center), and the early Pleistocene (1.0–2.6 Ma; right). Blue lines indicate the PSD of the standardized $\delta^{18}\text{O}$ records, while dashed and dotted black lines denote the 95% and 90% confidence levels, respectively, against an AR(1) benchmark. Vertical dashed lines highlight key periodicities: the canonical eccentricity (95 kyr), obliquity (41 kyr), and precession (23 kyr) cycles, as well as the sub-harmonics analyzed in this study (82, 76, and 52 kyr). The series are linearly detrended over the analysis period. All analyses are performed using the pyleoclim (version 1.2.0) [18].

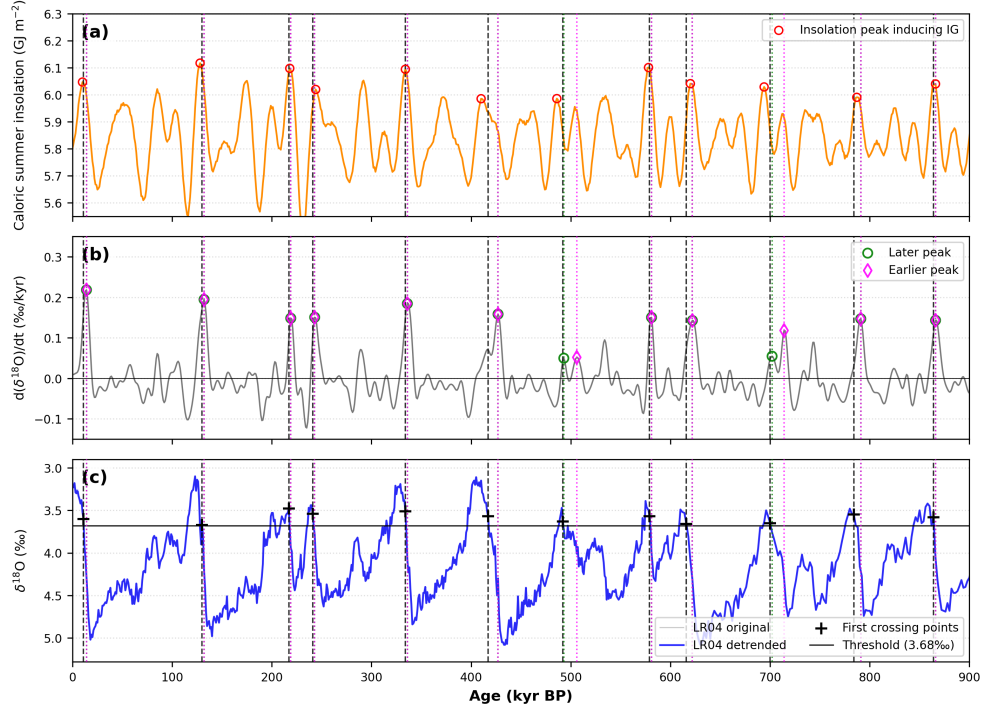


Fig. S11 Detailed deglaciation analysis and timing of interglacial onsets (0–900 ka). (a) Caloric summer insolation at 65°N [2, 3]. Red open circles denote the interglacial-inducing insolation peaks [1] (see Methods). (b) The rate of change in benthic $\delta^{18}\text{O}$ ($d(\delta^{18}\text{O})/dt$) derived from the 10-kyr smoothed LR04 $\delta^{18}\text{O}$ record. Green circles and magenta diamonds highlight the local maxima in the deglaciation rate, representing later and earlier phases of ice-sheet retreat, respectively. (c) Benthic $\delta^{18}\text{O}$ records from the LR04 stack. The original record (light gray) is shown alongside the detrended series [1] (blue line) used for threshold analysis (see Methods). Black crosses ('+') mark the first crossing points where the detrended $\delta^{18}\text{O}$ values exceed the 3.68‰ threshold, defining the onset of interglacial conditions. Vertical dashed lines (black) and dotted lines (green and magenta) indicate the timings of threshold crossings and peak deglaciation rates, respectively, highlighting the phase relationship between each insolation peak and climate response.

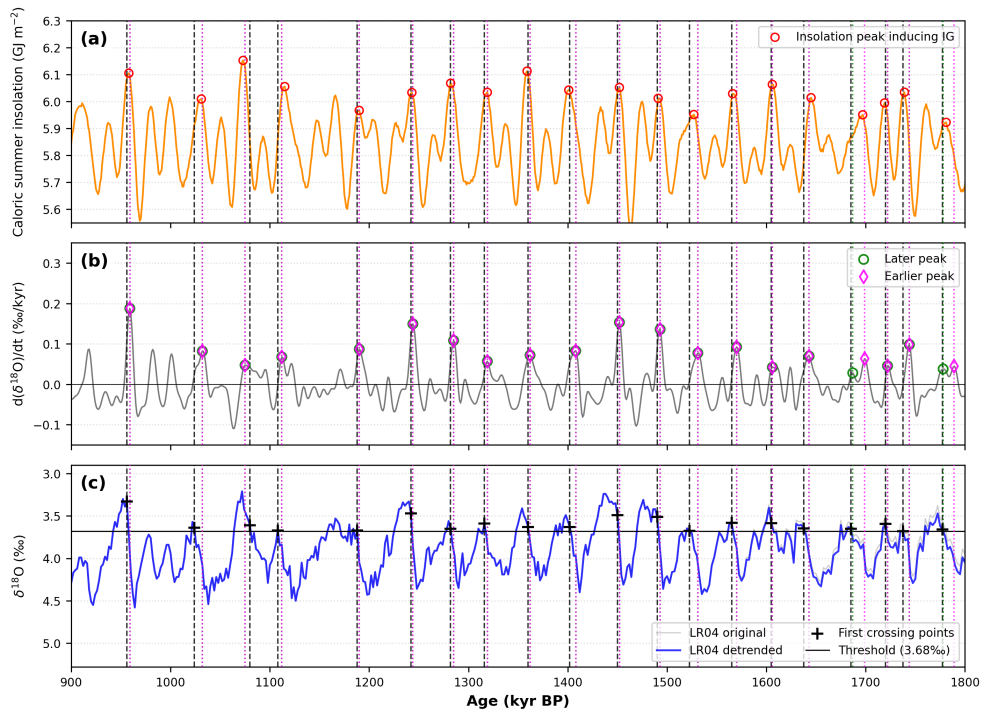


Fig. S12 Detailed deglaciation analysis and timing of interglacial onsets (900–1800 ka). See caption in Fig. S11.

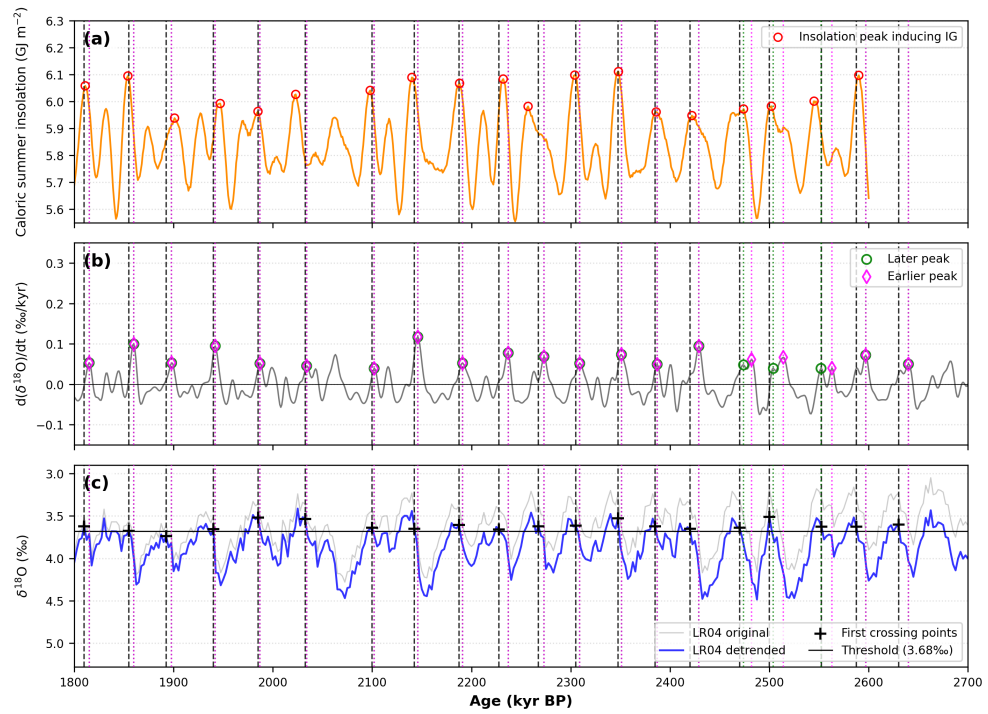


Fig. S13 Detailed deglaciation analysis and timing of interglacial onsets (1800–2700 ka). See caption in Fig. S11.

Relationship between Eccentricity and Precession Duration

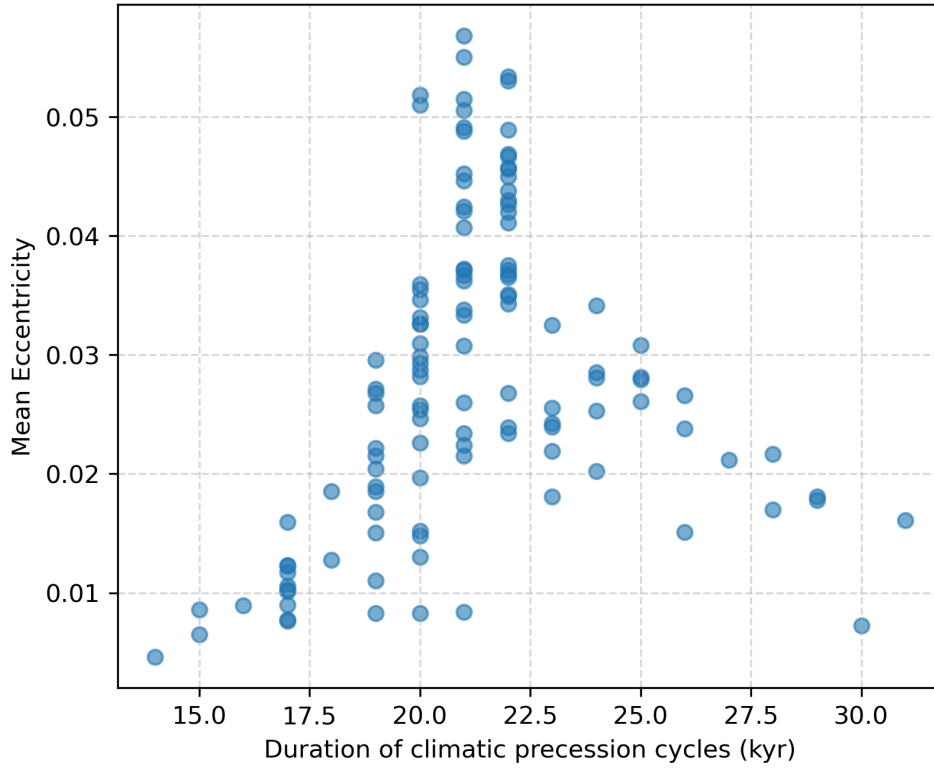


Fig. S14 Relationship between eccentricity and the duration of climatic precession cycles. The duration of climatic precession cycle is calculated from the spacing between successive precession minima. The local mean of eccentricity is calculated over successive precession minima.

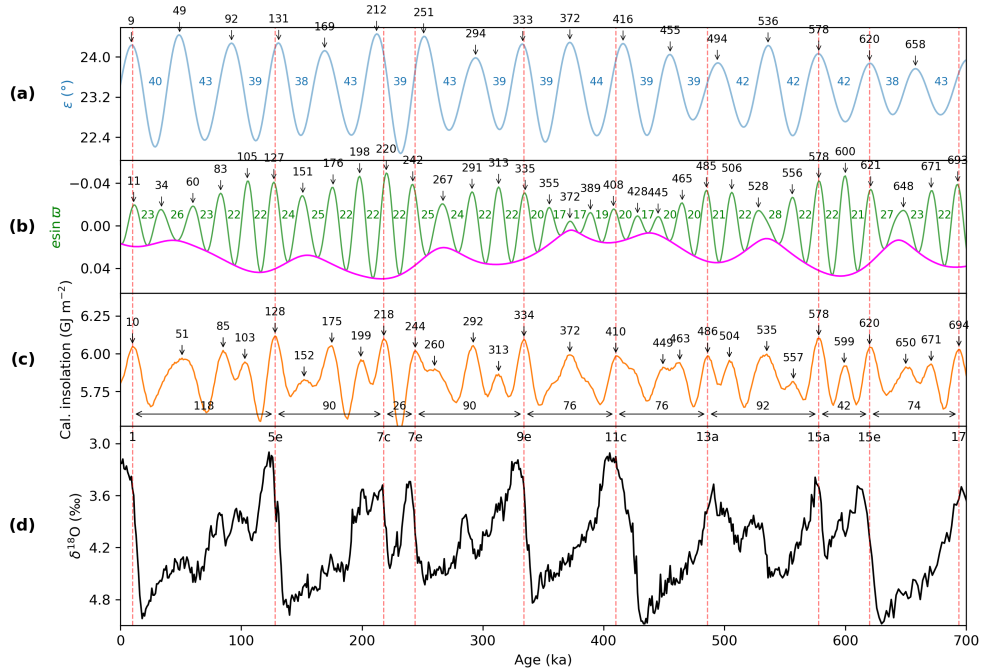


Fig. S15 Orbital forcing and glacial-interglacial cycles over the last 700 kyr. (a) Obliquity (ε) with peak ages (ka) indicated by arrows. Peak-to-peak spacings are shown in blue between consecutive peaks. (b) Climatic precession ($e \sin \varpi$, green) and eccentricity (e , magenta). Note that the $e \sin \varpi$ axis is inverted to align with insolation peaks. Peak-to-peak spacings are shown in green between consecutive minima. (c) Caloric summer half-year insolation at 65°N [2, 3]. Horizontal double-headed arrows indicate the interglacial spacings (T_{ins}), where values correspond to the spacings between interglacial-inducing insolation maxima. (d) LR04 $\delta^{18}\text{O}$ stack [11]. Numbers at the top denote Marine Isotope Stages (MIS). Vertical red dashed lines across all panels mark the timing of insolation peaks that induced interglacials [1]. The orbital solutions are from Laskar et al. (2004) [4].

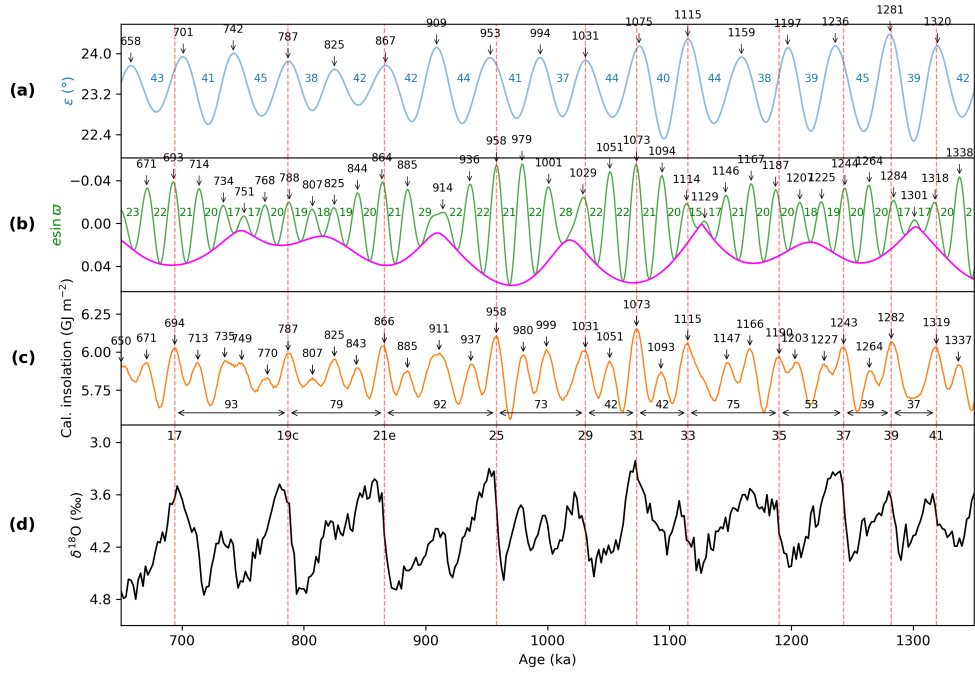


Fig. S16 Orbital forcing and glacial-interglacial cycles from 650 to 1350 ka. (a) Obliquity (ε) with peak ages (ka) indicated by arrows. Peak-to-peak spacings are shown in blue between consecutive peaks. (b) Climatic precession ($e \sin \varpi$, green) and eccentricity (e , magenta). Note that the $e \sin \varpi$ axis is inverted to align with insolation peaks. Peak-to-peak spacings are shown in green between consecutive minima. (c) Caloric summer half-year insolation at 65°N [2, 3]. Horizontal double-headed arrows indicate the interglacial spacings (T_{ins}), where values correspond to the spacings between interglacial-inducing insolation maxima. (d) LR04 $\delta^{18}\text{O}$ stack [11]. Numbers at the top denote Marine Isotope Stages (MIS). Vertical red dashed lines across all panels mark the timing of insolation peaks that induced interglacials [1]. The orbital solutions are from Laskar et al. (2004) [4].

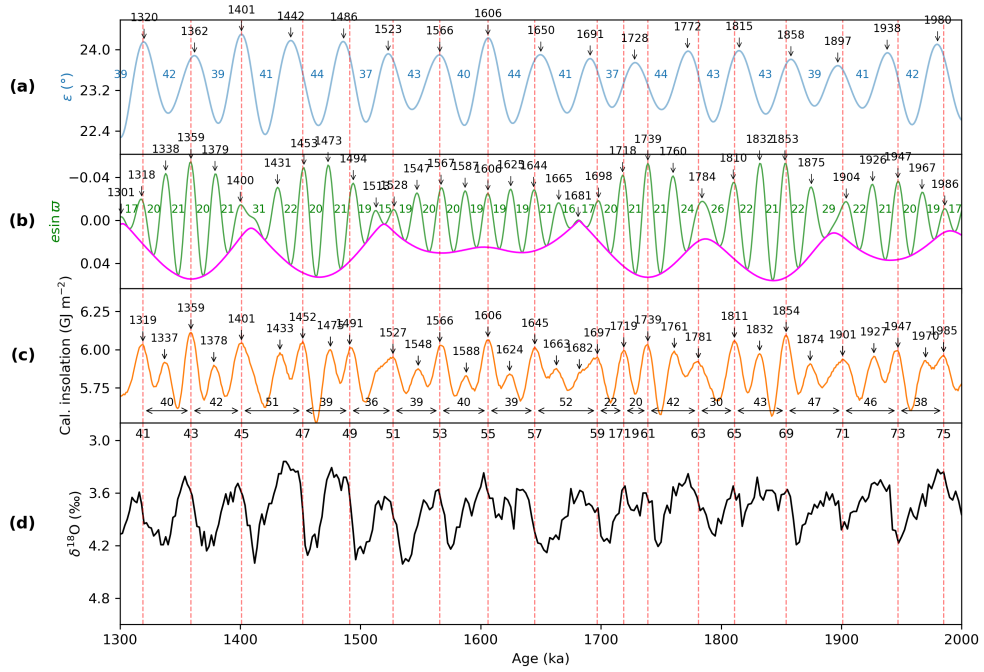


Fig. S17 Orbital forcing and glacial-interglacial cycles from 1300 to 2000 ka. (a) Obliquity (ϵ) with peak ages (ka) indicated by arrows. Peak-to-peak spacings are shown in blue between consecutive peaks. (b) Climatic precession ($e \sin \omega$, green) and eccentricity (e , magenta). Note that the $e \sin \omega$ axis is inverted to align with insolation peaks. Peak-to-peak spacings are shown in green between consecutive minima. (c) Caloric summer half-year insolation at 65°N [2, 3]. Horizontal double-headed arrows indicate the interglacial spacings (T_{ins}), where values correspond to the spacings between interglacial-inducing insolation maxima. (d) LR04 $\delta^{18}\text{O}$ stack [11]. Numbers at the top denote Marine Isotope Stages (MIS). Vertical red dashed lines across all panels mark the timing of insolation peaks that induced interglacials [1]. The orbital solutions are from Laskar et al. (2004) [4].

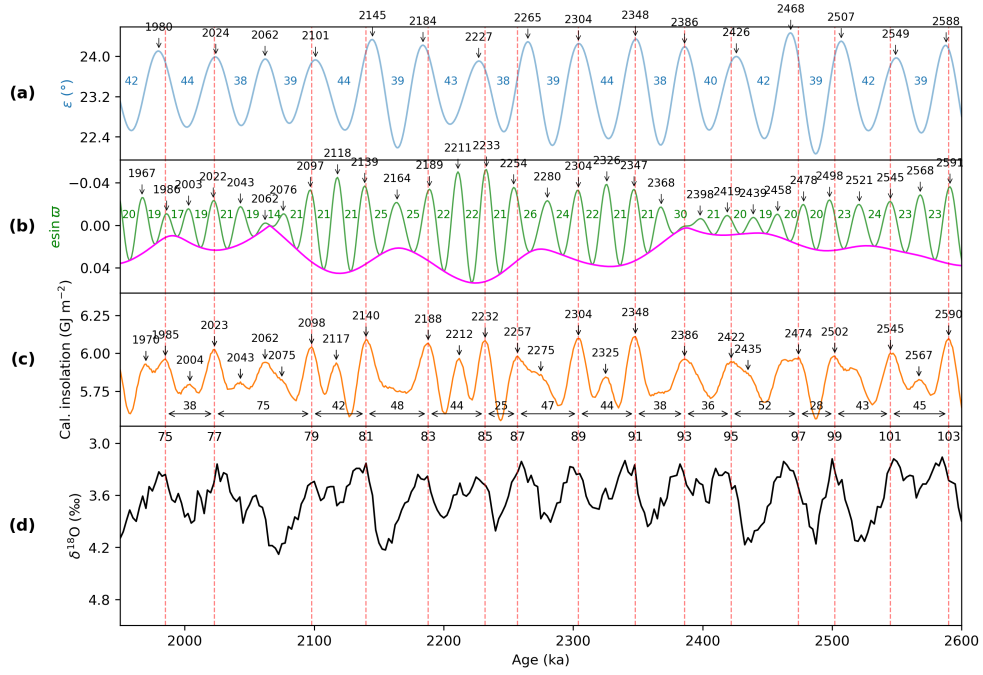


Fig. S18 Orbital forcing and glacial-interglacial cycles from 1950 to 2600 ka. (a) Obliquity (ε) with peak ages (ka) indicated by arrows. Peak-to-peak spacings are shown in blue between consecutive peaks. (b) Climatic precession ($e \sin \omega$, green) and eccentricity (e , magenta). Note that the $e \sin \omega$ axis is inverted to align with insolation peaks. Peak-to-peak spacings are shown in green between consecutive minima. (c) Caloric summer half-year insolation at 65°N [2, 3]. Horizontal double-headed arrows indicate the interglacial spacings (T_{ins}), where values correspond to the spacings between interglacial-inducing insolation maxima. (d) LR04 $\delta^{18}\text{O}$ stack [11]. Numbers at the top denote Marine Isotope Stages (MIS). Vertical red dashed lines across all panels mark the timing of insolation peaks that induced interglacials [1]. The orbital solutions are from Laskar et al. (2004) [4].

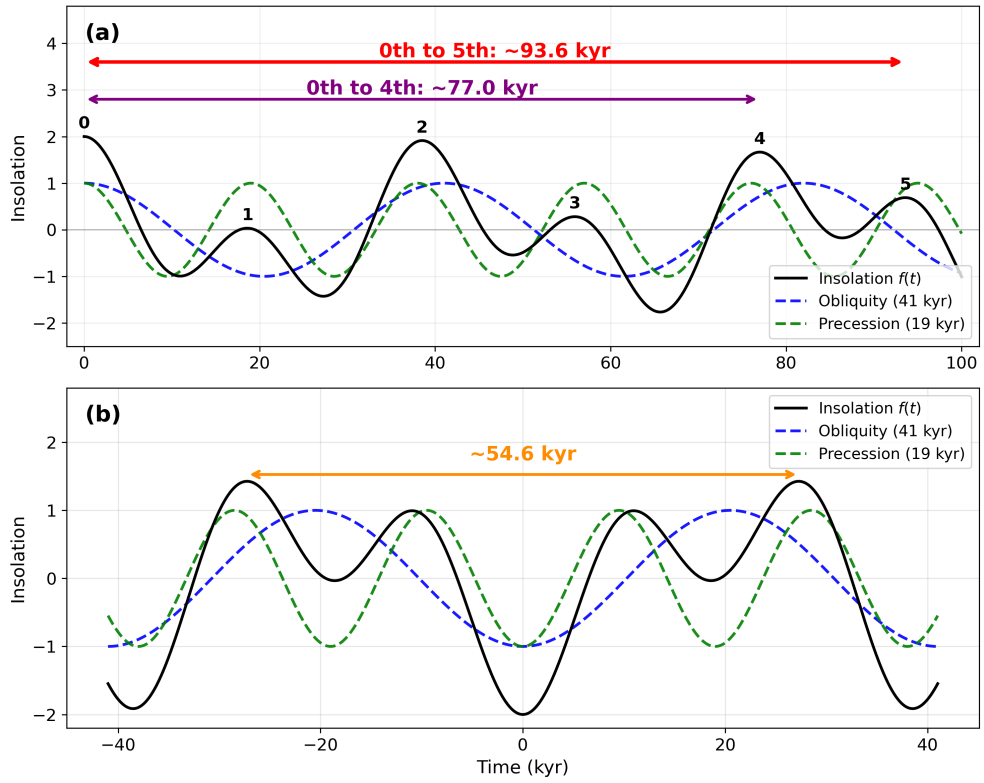


Fig. S19 Schematic representation of an insolation curve approximated by two harmonic components. The insolation curve is assumed to be represented as the sum of two harmonic components: $\cos(2\pi t/19)$ (climatic precession) and $\cos(2\pi t/41)$ (obliquity). (a) The insolation curve is given by $f(t) = \cos(2\pi t/19) + \cos(2\pi t/41)$. (b) The insolation curve is given by $f(t) = -\cos(2\pi t/19) - \cos(2\pi t/41)$.

Supporting Information Table S1 for "Beyond the 100-kyr and 41-kyr dichotomy: ~76-kyr and ~52-kyr signals and forbidden periodicities" by Takahito Mitsui

Creator: Takahito Mitsui (Juntendo University). (email: takahito321ATgmail.com)

Date: 2 April 2026

Description:

This sheet shows the calculation of the insolation-based inter-deglaciation intervals (T_{ins}) by using the approximation formulae described in Supporting Information document.

The colitic summer half-year insolation at 65N is chosen as the insolation metric following Tzedakis et al. Nature (2017). It is calculated based on the orbital solution of Laskar et al. A&A (2004) using R-package 'Palinsol' created by Michel Crucifix.

The insolation-based inter-deglaciation interval (T_{ins}) between two interglacials (called "start" and "end" below) is approximately given by the spacing between two insolation peaks that induce interglacials.

Marine Isotope Stage (MIS) of interglacial "end"	Marine Isotope Stage (MIS) of interglacial "start"	Insolation peak "end" (ka)	Insolation peak "start" (ka)	Actual inter-deglaciation interval (T_{ins}) (kyr)	Precession (esin) peak "end" (ka)	Precession (esin) peak "start" (ka)	Number of precession cycles	Local-mean precession period T_p (kyr)	Oblliquity peak "end" (ka)	Oblliquity peak "start" (ka)	Number of obliquity cycles	Local-mean obliquity period (kyr)	Formula type	Predicted Inter-deglaciation interval (T_{ins}) (kyr)	Difference = predicted T_{ins} - actual T_{ins} (kyr)	T_{later} (kyr)	$T_{earlier}$ (kyr)
1	5e	10	128	118	11	127	5	23.2	9	131	3	40.66666667	5a	117.4095046	-0.590495389	118	118
5e	7c	128	218	90	127	220	4	23.25	131	212	2	40.5	4a	90.75253717	0.752537167	87	87
7c	7e	218	244	26	220	242	1	22	212	251	1	39	1b	25.63885892	-0.36114108	24	24
7e	9e	244	334	90	242	335	4	23.25	251	333	2	41	4a	90.8365547	0.83655466	93	93
9e	11c	334	410	76	335	408	4	18.25	333	416	2	41.5	4a	74.26141357	-1.738586426	91	91
11c	13a	410	486	76	408	485	4	19.25	416	494	2	39	pp	77	1	66	79
13a	15a	486	578	92	485	578	4	23.25	494	578	2	42	4a	91.13043353	-0.86956647	88	75
15a	15e	578	620	42	578	621	2	21.5	578	620	1	42	2a	42.7926566	0.792656604	41	41
15e	17	620	694	74	621	693	3	24	620	701	2	40.5	3a	74.10102939	0.101029386	80	92
17	19c	694	787	93	693	788	5	19	701	787	2	43	5a	93.76811957	0.768119566	89	77
19c	21e	787	866	79	788	864	4	19	787	867	2	40	4b	76.73089134	-2.26910866	75	75
21e	25	866	958	92	864	958	4	23.5	867	953	2	43	4a	92.31555016	0.315550159	93	93
25	29	958	1031	73	958	1029	3	23.66666667	953	1031	2	39	3a	72.7835095	-0.216490502	73	73
29	31	1031	1073	42	1029	1073	2	22	1031	1075	1	44	2a	44	2	43	43
31	33	1073	1115	42	1073	1114	2	20.5	1075	1115	1	40	2a	40.79230366	-1.207696343	37	37
33	35	1115	1190	75	1114	1187	4	18.25	1115	1197	2	41	4a	74.22310319	-0.776896814	78	78
35	37	1190	1243	53	1187	1244	3	19	1197	1236	1	39	3b	54.1564265	1.156426499	54	54
37	39	1243	1282	39	1244	1284	2	20	1236	1281	1	45	pp	40	1	41	41
39	41	1282	1319	37	1284	1318	2	17	1281	1320	1	39	2b	34.78698727	-2.213012733	34	34
41	43	1319	1359	40	1318	1359	2	20.5	1320	1362	1	42	pp	41	1	43	43
43	45	1359	1401	42	1359	1400	2	20.5	1362	1401	1	39	pp	41	-1	46	46
45	47	1401	1452	51	1400	1453	2	26.5	1401	1442	1	41	2a	50.04423465	-0.955765345	44	44
47	49	1452	1491	39	1453	1494	2	20.5	1442	1486	1	44	2c	39.73163334	0.731633338	41	41
49	51	1491	1527	36	1494	1528	2	17	1486	1523	1	37	pp	34	-2	38	38
51	53	1527	1566	39	1528	1567	2	19.5	1523	1566	1	43	2a	39.6628726	0.662872597	39	39
53	55	1566	1606	40	1567	1606	2	19.5	1566	1606	1	40	2a	39.19168569	-0.808314308	36	36
55	57	1606	1645	39	1606	1644	2	19	1606	1650	1	44	2a	38.87946221	-0.12053779	37	37
57	59	1645	1697	52	1644	1698	3	18	1650	1691	1	41	3b	52.08886632	0.088866322	44	56
59	1719	1697	1719	22	1698	1718	1	20	1691	1728	1	37	1c	21.5508926	-0.449107399	35	23
1719	61	1719	1739	20	1718	1739	1	21	1728	1728	0	#DIV/0!	pp	21	1	22	22
61	63	1739	1781	42	1739	1784	2	22.5	1728	1772	1	44	2c	43.11739279	1.117392788	34	45
63	65	1781	1811	30	1784	1810	1	26	1772	1815	1	43	1b	30.23605565	0.236055654	37	2
65	69	1811	1854	43	1810	1853	2	21.5	1815	1858	1	43	pp	43	0	45	45
69	71	1854	1901	47	1853	1904	2	25.5	1858	1897	1	39	2b	47.48572001	0.485720005	38	38
71	73	1901	1947	46	1904	1947	2	21.5	1897	1938	1	41	2d	44.86553125	-1.134468748	44	44
73	75	1947	1985	38	1947	1986	2	19.5	1938	1980	1	42	2c	37.81281134	-0.187188656	45	45
75	77	1985	2023	38	1986	2022	2	18	1980	2024	1	44	2b	37.11082651	-0.889173493	47	47
77	79	2023	2098	75	2022	2097	4	18.75	2024	2101	2	38.5	4b	75.38269763	0.382697632	68	68
79	81	2098	2140	42	2097	2139	2	21	2101	2145	1	44	pp	42	0	44	44
81	83	2140	2188	48	2139	2189	2	25	2145	2184	1	39	2b	46.86370843	-1.136291572	45	45
83	85	2188	2232	44	2189	2233	2	22	2184	2227	1	43	2b	43.79261153	-0.207388473	46	46
85	87	2232	2257	25	2233	2254	1	21	2227	2265	1	38	1b	24.46929504	-0.53070496	3	36
87	89	2257	2304	47	2254	2304	2	25	2265	2304	1	39	2a	47.27718819	0.277188193	36	36
89	91	2304	2348	44	2304	2347	2	21.5	2304	2348	1	44	2a	43.19246791	-0.807532094	42	42
91	93	2348	2386	38	2347	2398	2	25.5	2348	2386	1	38	O2-(P1+C)	38.5	0.5	36	36
93	95	2386	2422	36	2398	2419	1	21	2386	2426	1	40	(O2+P2)/	36.5	0.5	42	42
95	97	2422	2474	52	2419	2478	3	19.66666667	2426	2468	1	42	3b*	51.96142631	-0.038573691	45	53
97	99	2474	2502	28	2478	2498	1	20	2468	2507	1	39	1b*	27.94484616	-0.055153836	30	32
99	101	2502	2545	43	2498	2545	2	23.5	2507	2549	1	42	2c	45.05090417	2.050904171	48	49
101	103	2545	2590	45	2545	2591	2	23	2549	2588	1	39	2b	44.21662793	-0.78337207	45	34

Note: Special rules are employed for MIS 99-97, 97-95, 95-93, and 93-91, where eccentricity is particularly low. See Supplementary Note.